JOURNAL OF GEOPHYSICAL RESEARCH, VOL. 112, E04002, doi:10.1029/2006JE002777, 2007

Martian Dunite NWA 2737: Petrographic constraints on geological history, shock events, and olivine color

Allan H. Treiman,[1] M. Darby Dyar,[2] Molly McCanta,[1] Sarah K. Noble,[3] and Carle M. Pieters[4]

Received 16 June 2006; revised 26 July 2006; accepted 1 September 2006; published 17 April 2007.

[1] Meteorite Northwest Africa (NWA) 2737 is the second known chassignite, an olivine-rich igneous rock with mineral compositions and isotopic ratios that suggest it formed on Mars. NWA 2737 consists of ~85% vol. olivine (Mg#, molar Mg/(Mg + Fe), of 78.3 ± 0.4%), which is notable because it is black in hand sample and brown in thin section. Other minerals include chromite, pyroxenes (augite, pigeonite, orthopyroxene), and diaplectic glass of alkali-feldspar composition. Aqueous alteration is minimal and appears only as slight dissolution of glass. NWA 2737 formed by accumulation of olivine and chromite from a basaltic magma; the other minerals represent magma trapped among the cumulus grains. Minerals are compositionally homogeneous, consistent with chemical equilibration in late and postigneous cooling. Two-pyroxene thermometry gives equilibration temperatures ~1150°C, implying a significant time spent at the basalt solidus. Olivine-spinel-pyroxene equilibria give ~825°C (possibly the T of mesostasis crystallization) at an oxidation state of ~QMF-1. This oxidation state is consistent with low Fe^{3+} in olivine (determined by EMP, Mössbauer spectra, and synchrotron micro-XANES spectroscopy) and with ~10% of the iron in pyroxene being Fe^{3+}. NWA 2737 experienced two shock events. The first shock, to stage S5–S6, affected the olivine by producing in it planar deformation features, intense mosaicism and lattice strain, and abundant droplets of iron-nickel metal, 5–15 nm in diameter. At this stage the olivine became deeply colored, i.e., strongly absorbing at visible and near-infrared (NIR) wavelengths. This shock event and its thermal pulse probably occurred at ~170 Ma, the Ar-Ar age of NWA 2737. The colored olivine is cut by ribbons of coarser, uncolored olivine with long axes along [100] and shorter axes on {021} planes: These are consistent with the easy slip law for olivine [100]{021}, which is activated at moderate strain rate at high temperature. Within these ribbons the olivine was coarsened and the iron metal globules coalesced to micron-sized grains. The ribbons also are mosaicized and cut by planar fractures, which bespeak a second shock event, possibly that of ejection from Mars. The deeply colored olivine in NWA 2737 is unusual and represents a new "ground truth" type for remote sensing of Mars. Understanding the occurrence of the brown color in olivine in NWA 2737 places important constraints on interpretation of optical measurements.

Citation: Treiman, A. H., M. D. Dyar, M. McCanta, S. K. Noble, and C. M. Pieters (2007), Martian Dunite NWA 2737: Petrographic constraints on geological history, shock events, and olivine color, *J. Geophys. Res.*, *112*, E04002, doi:10.1029/2006JE002777.

1. Introduction

[2] The Martian (SNC) meteorites are critically important for understanding Mars, because they provide details of petrography and chemistry that cannot be measured in situ, and they provide "ground truths" for spectral analyses from the Martian surface using Mössbauer, thermal emission, and visible, near-IR, and mid-IR reflectance techniques. The recently discovered NWA 2737 meteorite is the second known chassignite, an olivine-rich igneous cumulate rock. The eponymous Chassigny has gained importance recently by the suggestion that it and other Martian meteorites have spectral signatures that match those of the Syrtis Major volcano on Mars [*Harvey and Hamilton*, 2005], and so may have originated in that area. NWA 2737 could also have come from that area, and (more generally) is another example of an olivine-rich lithology from Mars. Here, we present petrologic and mineral compositional data, TEM

[1]Lunar and Planetary Institute, Houston, Texas, USA.
[2]Department of Astronomy, Mount Holyoke College, South Hadley, Massachusetts, USA.
[3]ARES Division, Johnson Space Center, Houston, Texas, USA.
[4]Department of Geological Sciences, Brown University, Providence, Rhode Island, USA.

0148-0227/07/2006JE002777$09.00

Table 1. Modal (Volume %) Mineral Proportions

Phase %	This Paper	*Beck et al.* [2006]	*Mikouchi et al.* [2005]
Olivine	85.1	89.6	89
Chromite	2.9	4.6	3
Low-Ca pyroxene	4.0	1.0	3
Augite	5.0	3.1	4
Glass	2.2	–	1
Sanidine	–	1.6	–
Carbonate	0.9	–	–
Phosphate	–	0.2	–
Points	2050	–	–

imagery, Mössbauer spectrometry, and synchrotron micro-XANES data on NWA 2737 to constrain its geological history and origin, and as a basis for EM spectroscopic measurements such as are being taken by orbital and lander spacecraft on Mars. In this way, we hope to provide additional "ground truth" on Martian rocks to help interpret orbital data.

[3] More than thirty meteorites from Mars are known, and all are basalts or were derived from basaltic magma. The Martian origin of these samples is confirmed by the similarity of their isotopic and chemical compositions to in situ analyses at Mars, and by theoretical considerations of the evolution of terrestrial planets versus asteroids [e.g., *Bogard and Johnson*, 1983; *Becker and Pepin*, 1984; reviewed in *Treiman et al.*, 2000]. Several types of Martian meteorites are known, all representing mafic to ultramafic igneous rocks. Shergottites include basalts proper (with and without olivine) and lherzolitic cumulates from basalt. Nakhlites are augite cumulates from basaltic magmas, and chassignites are olivine cumulates (dunites) from basaltic magmas. These three groups constitute the early "SNC" eponymous label for the Martian meteorites. In addition, the Martian orthopyroxenite ALH84001 is also a cumulate from a basaltic magma.

[4] The Chassigny meteorite was the only member of the chassignite class until 2005, when NWA 2737 was recognized as the second [*Beck et al.*, 2005, 2006; *Mikouchi et al.*, 2005; this study]. Like Chassigny, NWA 2737 is an olivine cumulate with intercumulus pyroxenes, feldspars, and oxides; the inference of its Martian origin is based on its mineralogy and mineral chemistry (see *Treiman et al.* [2000]), a crystallization age of ~1.35 Ga, and its origin from a highly differentiated mantle source [*Misawa et al.*, 2005a], its Fe/Mn ratio [*Mikouchi et al.*, 2005; *Beck et al.*, 2006], and its oxygen isotope composition [*Beck et al.*, 2006]. Data here affirm a Martian origin for NWA 2737 especially that the FeO/MnO ratios in its olivine, orthopyroxene, and augite (49, 65, and 64 respectively) that match those of other Martian rocks, and are distinct from those in lunar, terrestrial, and most asteroidal basalts [e.g., *Papike et al.*, 2003; *Karner et al.*, 2003].

[5] The purpose of this work is to describe the mineralogy and geologic history of NWA 2737, especially as it may relate to remote sensing. Many spacecraft are now orbiting Mars with a wide variety of remote sensing instruments, and NWA 2737 provides yet another piece of ground truth to calibrate those remote measurements. NWA 2737 is particularly interesting in this regard, because it is very highly colored in visible wavelengths and quite distinct from the typical green color of olivine-rich rocks. Electromagnetic spectral measurements of NWA 2737 will be presented in a companion paper C. M. Pieters et al., Martian dunite NWA 2737: Electromagnetic spectroscopy and implications for remote sensing, submitted to *Journal of Geophysical Research*, 2007; hereinafter referred to as Pieters et al., submitted manuscript.

2. Sample Preparation and Methods

[6] A 1.75 g fragment of NWA 2737 was purchased from the finders, Bruno Fectay and Carine Bidaut of *La Memoire de la Terre*. That fragment was mounted for cutting with Crystalbond adhesive at the Lunar and Planetary Institute (LPI) and halved with a wafering saw using distilled water for lubrication and cooling. The portion with Crystalbond was used to prepare a polished thin section on silica glass. Water and rock chips from these cuts were evaporated to dryness and saved for spectroscopy and bulk chemistry, along with samples of cut Crystalbond adhesive and epoxy for comparison. This thin section was used for petrographic descriptions, mineral abundances (Table 1), and chemical analysis. To constrain the valence state and site occupancy of iron in the minerals of NWA 2737, coauthor McCanta also acquired synchrotron Fe X-ray near-edge absorption spectra (SmX) from the thin section.

[7] The chip of NWA 2737 without Crystalbond or epoxy, ~0.5 gm, was reserved for bulk spectroscopic measurements (Pieters et al., submitted manuscript). After these EM spectral studies, the bulk rock and mineral powders were returned to Dyar for acquisition of Mössbauer spectra.

[8] Petrographic descriptions were made from optical and backscattered electron (BSE) studies of the thin section. Crystallographic orientations of features in olivine were determined by conoscopic examination of interference figures under crossed polarized light. Mineral chemical analyses (Tables 2 and 3) were obtained by electron microprobe with the Cameca SX100 in the ARES division, Johnson Space Center. Analytical conditions were 15 kV accelerating potential, a focused beam of 20 nA current, and peak count times of 20–30 sec for major elements and 60 sec for minor elements. Analytical standards used include spessartine for Mn, chromium metal and chromite for Cr, tugtupite for Cl, Durango apatite for P, fluorite for F, pure metals for V and Co, NiO for Ni, and Spring Hill kaersutite for the remaining elements. Analyses were verified by analyzing the standards and selected reference materials as unknowns. Where possible, only "superior" analyses, having analytical totals between 99% and 100.5% and the proper mineral stoichiometry to within 0.5% (e.g., an olivine formula of $M_{2.000\pm0.010}Si_{1.000\pm0.005}$), were used. To reduce problems with alkali loss, glasses were analyzed with a defocused beam of nominal diameter 5 μm.

[9] To augment SmX and Mössbauer analyses, Fe^{3+} abundances in the olivine, pyroxenes, and chromite were calculated from EMP chemical analyses [e.g., *Banfield et al.*, 1992; *Dyar et al.*, 2005]. This calculation assumes that stoichiometry is fulfilled (no vacant sites), all major and minor elements have been analyzed (e.g., no Li), and iron is the only element present in multiple valence states. The chemical analysis is then normalized to the proper number

Table 2. Mineral Chemical Compositions and Cation Proportions[a]

Element	Olivine	Augite	Pigeonite	OPX	Chromite 1	Chromite 2
SiO_2	38.77	53.21	55.32	55.23	0.01	0.01
TiO_2	0.03	0.33	0.12	0.12	2.61	1.78
Al_2O_3	0.10	1.22	0.57	0.66	9.77	8.16
Cr_2O_3	0.01	0.95	0.36	0.33	47.66	52.84
FeO	20.03	6.45	12.41	12.34	32.04	29.74
MnO	0.41	0.28	0.43	0.43	0.47	0.51
MgO	40.53	17.99	27.77	28.64	5.93	5.70
CaO	0.16	19.07	3.06	2.07	0.01	0.01
Na_2O	0.01	0.36	0.08	0.05	0.00	0.01
K_2O	0.00	0.01	0.00	0.00	0.00	0.00
Sum	100.06	99.85	100.13	99.91	98.52	98.74
Ca	0.004	0.748	0.117	0.079	0.001	0.000
Mg	1.554	0.982	1.479	1.523	0.295	0.285
Fe^{2+}	0.428	0.167	0.359	0.351	0.756	0.744
Fe^{3+}	0.003	0.030	0.012	0.018	0.138	0.089
Mn	0.009	0.009	0.013	0.013	0.013	0.015
Cr	0.001	0.053	0.011	0.010	1.346	1.499
Na	0.001	0.025	0.006	0.004	0.000	0.001
Al^{VI}	0.000	0.001	0.000	0.000	0.000	0.000
Al^{IV}	0.003	0.052	0.024	0.028	0.384	0.322
Ti	0.001	0.009	0.003	0.003	0.003	0.008
Si	0.997	1.948	1.976	1.971	0.000	0.000
Mg′ (%)	78.3 ± 0.4	83.3	80.0	80.5	–	–
$\%Fe^{3+}$ EMP	<1	15	3	5	15	11
$\%Fe^{3+}$ Möss	<3					
$\%Fe^{3+}$ XANES	14 ± 12					

[a]EMP analyses as described in text. n.a. = not analyzed; value of 0.00 means not detected. Olivine = average of 129 superior analyses (totals between 99% and 100.5%, without indication of contribution from other phases). Olivine analysis is normalized to 3 cations with +8 charge. Augite, Pigeonite, and OPX (orthopyroxene) are averages of 8, 21, and 20 analyses, respectively, normalized to 4 cations with +12 charge. Chromite normalized to 3 cations with +8 charge. Mg′(%) is molar Mg/(Mg + total Fe). $\%Fe^{3+}$ EMP is calculated as described in the text. $\%Fe^{3+}$ by Mössbauer and by XANES are from this work.

of cations in its formula (e.g., Table 2), and the total cation charge per formula unit is computed. If the total cation charge is less than the total anion charge per formula unit, the difference is calculated as Fe^{3+} (vs. Fe^{2+}). Fe^{3+} that is charge balanced by site vacancies or defects does not appear in the calculation as Fe^{3+}, but rather as a deficiency in the ratio of octahedral cations (e.g., Fe, Mg) to tetrahedral cations (Si). For example, the Fe^{3+} – vacancy olivine laihunite, $Fe^{2+}Fe^{3+}{}_2 \bullet (SiO_2)_2$ where "•" represents a vacant site, has Fe:Si = 1.5:1 while pure Fe^{2+} olivine (fayalite) has Fe:Si = 2:1. It must be remembered that calculating Fe^{3+} from microprobe analyses is semiquantitative at best, because the calculation ascribes all analytical imprecision and inaccuracy and all unanalyzed elements to Fe^{3+}.

[10] Amphiboles must be normalized differently [*Cosca et al.*, 1991]. The chemical formula for amphibole is nominally $A_{0-1}C_2M_5T_8O_{22}(OH, F, Cl, O)_2$, where the A site can hold K and Na, C sites can hold Ca, Na, and ferromagnesian cations, M sites can hold the ferromagnesian cations, Ti, Al, and Cr, and T sites hold Si and Al (and rarely Fe^{3+}). In calcic amphibole like that in NWA 2737, normalization is to M + T cations = 13 (i.e., Si + Al + Ti + Cr + Fe + Mg + Mn = 13), because the M and T sites do not support vacancies and because these C site is usually filled by Ca + Na. The normalization is checked to have Ca $\leq$ 2, Ca + Na = 2, Ca + Na + K $\leq$ 3, and Si + Al > 8 (Table 3). Fe^{3+} content cannot be calculated from EMP data alone, because EMP cannot analyze for hydrogen and thus cannot distinguish $Fe^{3+} - Fe^{2+}$ from $O^{2-} - OH^-$ exchanges.

[11] To constrain the ratios of Fe^{3+}/Fe^{2+} iron in minerals, synchrotron micro-XANES (SmX) spectra of amphibole and olivine in thin section were acquired at beam line X26A of the X-ray fluorescence microprobe facility, National Synchrotron Light Source (NSLS), Brookhaven National Laboratory. Analytical procedures followed *McCanta et al.* [2004a]. The locations and strengths of FeK pre-absorption-edge features were determined by scanning the energy of the incident X-ray beam in 0.3 eV increments from −10 to +20 eV relative to the main absorption edge at 7111 eV. Each energy interval was counted between 5 and 20 live seconds (depending on the intensity of the main edge signal. Each pre-edge spectrum was fitted to a third-order polynomial (background) plus a Gaussian function (peak envelope) for each pre-edge peak; the centroids of those peaks are reproducible to within 1%. XANES spectra are strongly affected by orientation of the crystal lattice relative to the X-ray beam [e.g., *Dyar et al.*, 2002]. For an overview of XANES spectroscopy and this application, see *Wilke et al.* [2001], *Mottana et al.* [2002] and *Dyar et al.* [2002].

[12] For Mössbauer analysis, approximately 10–20 mg of each sample were crushed to a fine powder with a sugar (sucrose) binder under acetone before mounting in a sample holder confined by cellophane tape. Spectra were acquired at 293K and at 12 or 14 K using a source of 30 mCi ^{57}Co in Rh on a WEB Research model W100 spectrometer equipped with a Janus closed cycle He refrigerator. Run times were 8–12 hours, and results were calibrated against α-Fe foil. Spectra were processed using the DIST_3D program, an

Table 3. Chemical Compositions of Other Phases[a]

Element	Inclusion Augite	Inclusion OPX	Inclusion Kaersutite	Inclusion Glass	Apatite	AFS Glass
SiO_2	48.53	52.72	42.36	69.88	0.86	68.84
TiO_2	1.84	0.43	6.69	0.10	0.01	0.13
Al_2O_3	5.38	2.14	12.27	22.61	0.54	20.40
Cr_2O_3	0.46	0.19	1.20	n.a.	0.01	n.a.
V_2O_3	0.06	n.a.	0.17	n.a.	0.00	n.a.
FeO	5.48	12.52	7.21	0.58	0.56	0.28
MnO	0.22	0.40	0.15	0.01	0.06	0.01
MgO	14.59	29.26	13.49	0.06	0.27	0.01
CaO	21.78	1.31	12.15	0.54	51.73	0.89
Na_2O	0.55	0.04	2.73	5.07	0.25	9.52
K_2O	0.00	0.00	0.43	3.67	0.02	3.23
P_2O_5	0.72	n.a.	0.14	n.a.	40.73	0.03
Cl	n.a.	n.a.	0.09	0.31	3.33	0.05
F	n.a.	n.a.	0.45	0.10	1.7	0.01
O = F, Cl	–	–	−0.21	−0.12	−1.5	–
Sum	99.55	100.07	99.39	101.80	100.08	102.61
Ca	0.863	0.056	1.893	–	4.873	0.044
Mg	0.804	1.498	2.925	–	0.036	0.001
Fe^{2+}	0.168	0.335	0.878	–	0.041	
Fe^{3+}	0.000	0.029	–	–	–	0.008
Mn	0.007	0.012	0.019	–	0.004	0.000
Cr	0.043	0.003	0.138	–	0.001	n.a.
Na	0.040	0.002	0.770	–	0.022	0.794
K	0.000	0.000	0.081	–	0.002	0.177
Al^{VI}	0.029	0.043	0.265	–	0.055	–
Al^{IV}	0.206	0.118	1.839	–	–	1.035
Ti	0.051	0.018	0.732	–	0.001	0.006
Si	1.794	1.882	6.161	–	0.077	2.958
P	–	n.a.	–		3.031	
Cl	n.a.	n.a.	0.023	–	0.497	n.a.
F	n.a.	n.a.	0.206	–	0.468	n.a.
Mg′ (%)	83	80	77	–	–	–
$\%Fe^{3+}$ EMP	0	9	–		–	–

[a]First four columns are average analyses of phases in a single magmatic inclusion in olivine. Augite and OPX normalized to 4 cations with +12 charge. Kaersutite amphibole normalized to [Si + Al + Ti + Fe + Mn + Mg + Cr] = 13, i.e., full occupancy of sites M1, M2, M3, T1, and T2. Apatite normalized to 5 divalent and monovalent cations. "AFS glass" = alkali feldspar glass in mesostasis, normalized to Si + Al + Fe = 4 cations. Mg′(%) is molar Mg/(Mg + total Fe). n.a. = not analyzed. $\%Fe^{3+}$ EMP calculated as described in the text.

implementation of software described in *Wivel and Mørup* [1981]. The program uses quadrupole splitting distributions with Lorentzian lineshapes and an assumed average correlation between the isomer shift (IS) and quadrupole shift (QS) in each of two valence states. Widths, isomer shifts, and quadrupole splittings of the doublets were allowed to vary. Errors on IS and QS for well-resolved peaks are usually ±0.02 mm/s; in heavily overlapped spectra such as those obtained in this study, the errors are probably ±0.05 mm/s. Errors on peak area depend on the extent of overlap with other peaks, but are generally ±3–5% absolute.

[13] Transmission electron microscopy (TEM) analyses of olivine were performed on grains selected from the mineral powder used for Mössbauer spectroscopy. These grains were crushed further, and mounted on holey carbon film suspended across a Cu grid. Analyses were performed by coauthor Noble at Johnson Space Center using a JEOL 2000-FX TEM, operating at 200 kV accelerating potential.

Figure 1. Thin section views of NWA 2737. Transmitted light, plane polarized; except as noted. (a) General texture. Olivine appears brown, with colorless bands and stripes; note euhedral termination of olivine in the center against mesostasis area (Figure 1c is rich in feldspathic glass). Chromite anhedra (black) within and among olivine grains. Magmatic inclusion (colorless circle) in brown olivine halfway down from image center. (b) Euhedral olivine grain (brown = VB) containing a round magmatic inclusion (mostly colorless). Inclusion contains kaersutite amphibole (brown grain in center of inclusion), aluminous pyroxenes, and feldspathic glass (Table 2). (c) Mesostasis texture, detail of area near top of Figure 1a. Bounding brown grains are olivine and colorless material is feldspathic glass in the shapes of feldspar crystals. Among the glass areas are low-Ca pyroxene, olivine, apatite, ilmenite, and Fe-sulfide. (d) Pyroxene (gray, white) filling space among olivine grains (dark, brown-yellow, and purple), transmitted light with crossed polarizers. Orthopyroxene (opx) is dark gray; yellow (left) and white (right) are augite (Figure 1a). Note interfingering of pyroxene species and optical continuity of the pyroxenes from the center of image to lower left. (e) Exsolution lamellae in augite, transmitted light with crossed polarizers. Olivine at top, appears white. Light-colored (high birefringence) patches in augite are secondary carbonate minerals along fractures. (f) Carbonate veinlet in olivine, transmitted light with crossed polarizers. Carbonate minerals appear white, and partially fill a crack that runs from upper left to lower right. Visually brown (VB) olivine is dark brown and tan, and visually colorless (VC) olivine is blue/purple; note subgrain boundary running from lower center left to upper center right; chromite is black.

Electron diffraction data were obtained by selected area (SAED) methods, using gold metal as a standard.

3. Petrography and Mineral Chemistry

[14] The analyzed sample of NWA 2737 is a dunite (Figure 1a) consisting, by volume, of ~85% olivine, ~9% pyroxene (augite, pigeonite, and orthopyroxene), ~3% chromite, and ~3% other phases including feldspathic and granitic glass, kaersutite amphibole, ilmenite, apatite, rutile, and Fe-sulfide (Table 1). Our portion of this meteorite does not have fusion crust. This sample is truly NWA 2737, as its textures, mineralogy, and mineral chemistry match those in the formal description of the meteorite [*Russell et al.*, 2005], in preliminary reports [*Beck et al.*, 2005; *Mikouchi*, 2005; *Mikouchi et al.*, 2005], and in a peer-reviewed publication [*Beck et al.*, 2006].

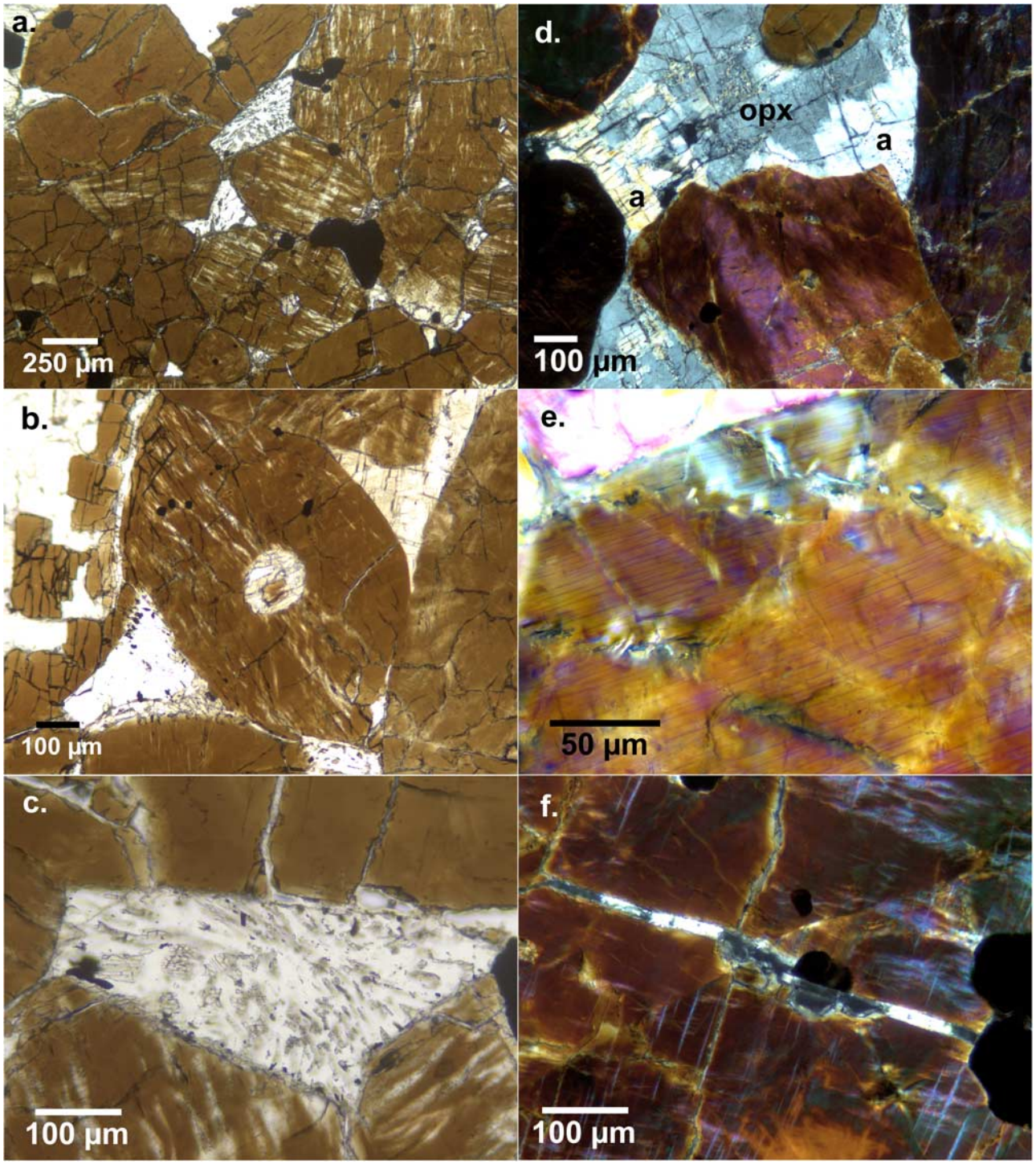

Figure 1

[15] The petrography and chemistry of NWA 2737 have been reported briefly [*Beck et al.*, 2006], and we confirm that report. NWA 2737 is an olivine-rich rock that appears to be an igneous cumulate of olivine and chromite crystals, with interstitial pyroxenes (augite, pigeonite, and orthopyroxene) and fine-grained mesostasis (composed mostly of alkali feldspar glass). The rock shows signs of intense shock, but not to melting (only one possible shock-melt pod was noted). NWA 2737 is not brecciated, and does not show microfaults. Here, we focus on the petrologic aspects of NWA 2737 that contribute to understanding its spectral properties. Thus we emphasize olivine, the most abundant mineral, and its brown color that is prominent in visible and near-infrared (NIR) reflectance spectra.

3.1. Olivine

[16] Olivine grains up to ~2 mm long and ~1.5 mm wide compose the bulk of NWA 2737, with the other minerals and materials among or inside them (Figures 1a and 1b). Where olivine grains abut mesostasis, they show planar, crystallographically controlled edges with the typical elongation on their b axes (Figures 1a–1d). Olivine grains abutting other olivine grains have slightly curved or planar boundaries (Figures 1a, 1d, and 1e), while olivine grains abutting pyroxene grains have boundaries with tighter curves (Figure 1d). Olivine grains contain rare magmatic inclusions (composed of silicate glass and minerals, Figure 1b), and numerous inclusions of chromite, 5–100 μm across, with selvages of colorless silicate glass (Figure 2d). There appears to be a continuum between chromite inclusions and similar-sized magmatic inclusions. The NWA 2737 olivine grains do not contain "symplectic exsolution lamellae" of augite and magnetite, as are found in several other Martian meteorites [e.g., *Greshake et al.*, 1998; *Mikouchi et al.*, 2000; *Treiman*, 2005]. The olivine shows almost no indication of weathering or interaction with aqueous fluids, except for rusty stains on fractures in a few spots.

[17] Olivine in NWA 2737 occurs in two colors (Figures 1 and 2): visually clear (VC) and visually brown (VB) in thin section: These names are chosen for consistency with the multispectral studies by Pieters et al. (submitted manuscript). VB olivine is dominant, as reflected in the black color of NWA2737 chips. Textures of VB and VC olivine are discussed below. Oddly, the VB brown olivine appears slightly brighter in BSE imagery than the VC colorless olivine (Figures 2c and 2d). This difference might imply that the VB olivine has a slightly greater electron density than the VC, i.e., is a denser phase or contains a denser phase, as suggested by electron diffractions results and Raman spectra [*Reynard et al.*, 2006a].

3.1.1. Visually Brown (VB) Olivine

[18] Each olivine grain in NWA 2737 is brown in thin section, except where cut by the visually colorless (VC) olivine described below. Within the brown areas, the color appears constant across each grain; there are no visible variations core-to-rim [e.g., *Bauer*, 1979], or associations with other mineral grains or inclusions.

[19] At high optical magnification, the brown olivine is cut by darker, micron-scale stripes or lamellae oriented on crystallographic directions, especially on {010} planes (Figure 2f). These lamellae are discontinuous, each being at most one hundred microns long, and are spread evenly through the brown areas. Optically, the lamellae are marked by tiny opaque grains, which range from a few microns across down to the limit of optical resolution. The lamellae can be recognized in enhanced BSE imagery of brown olivine as discontinuous darker stripes (lower electron density), a micron or less in width, that intersect visually clear olivine lenses at ~45° angles. These lamellae appear as short cracks of ~50 μm length, spaced ~10 μm apart, oriented along {010} and {001} planes (Figure 2a). These structures do not penetrate into the VC olivine, but terminate abruptly at their edges.

[20] Brown olivine is divided into subgrains of a few degrees of optical dispersion from the average optical orientation. This dispersion is apparent in TEM images as areas of lattice misorientations, and in electron diffraction patterns as a broadening and arcing of diffraction spots. A

Figure 2. Olivine textures in NWA 2737. Transmitted light, plane polarized except as noted. (a) Visually colorless (VC) and brown olivine (VB), viewed down the crystallographic a axis of an olivine grain. Lenticular areas of VC olivine are oriented at right angles to each other and at 45° to the optical extinction directions, implying an orientation approximately on {021} planes. Planar deformation features (pdfs), are dark lines along {100} and {001}. (b) VC and VB olivine in a grain just below the center of Figure 1a. Nearly same scene as Figure 2c. Section plane is nearly perpendicular to one set of VC ribbons (approximately horizontal), and at a low angle to the other set (see Figure 2a). Note sharp boundaries of VC lenses and stripes and the small opaque grains in them and concentrated at their boundaries. (c) Backscattered electron (BSE) image: textures of VC and VB olivine in a grain just below the center of Figure 1a; nearly same scene as Figure 2b. Areas of VC olivine (see Figure 2b) have a darker tone (i.e., lower BSE yield) than areas of VB olivine. VC olivine (darker) contains abundant small cracks (black lines) approximately along {010}, which tend to terminate at the brown olivine (brighter). White line is location of analytical traverse in Figure 4. (d) VC and VB olivine in grain of Figure 1d, backscattered electron (BSE) image; a portion of the grain in Figure 1d rotated ~180°. Grain has crystallographic b axis near the thin section plane. VC olivine has a darker tone (i.e., lower BSE yield) than does VB. VC areas (darker) are extensively cracked; cracks terminate at the VB olivine (brighter). White areas are chromite, the smaller of which (down left of center) are associated with small magmatic inclusions. A larger magmatic inclusion sits just above image center. (e) "Flames" of VB and VC olivine. "Flames" are generally oriented parallel to the elongations of olivine grains (crystallographic b), as on the left and right of the image. In the image center the "flames" bend at grain boundaries and deviate from crystallographic directions. (f) Planar deformation features (pdf) in olivine, in gray scale with enhanced contrast. Pdf are dark stripes, on crystallographic {010} planes, running bottom left to top right in right side of image. Note small dark specks that mark the modulation of color. Grain viewed nearly down [100] or crystallographic a, as in Figure 2a. VC lenses oriented up, down, and across are on {021}.

few olivine grains also show subgrains of slightly different orientation, separated by long planar boundaries: These resemble kink band boundaries common in Earth mantle rocks (Figure 1f).

[21] Most VB olivine contains few cracks, even though adjacent VC olivine can be heavily cracked.

[22] Most of the olivine fragments investigated with TEM showed strongly mottled contrast typical of lattice strain and subgrains, and abundant rounded inclusions, ~5–20 nm across, of higher electron density (Figures 3a and 3c). This material, because of its abundance, is inferred to be the VB olivine. Electron diffraction patterns of these grains can be complex (Figure 3d), with diffuse diffractions, arcs of diffractions suggesting multiple subgrains, and doubling of some diffractions suggesting an additional phase. The strongest diffractions are from olivine, with $\underline{a}$ = 0.477 nm (Figure 3d). This value of a is consistent with olivine of ~Fo_{80} [*Akimoto et al.*, 1976], which compares well with the

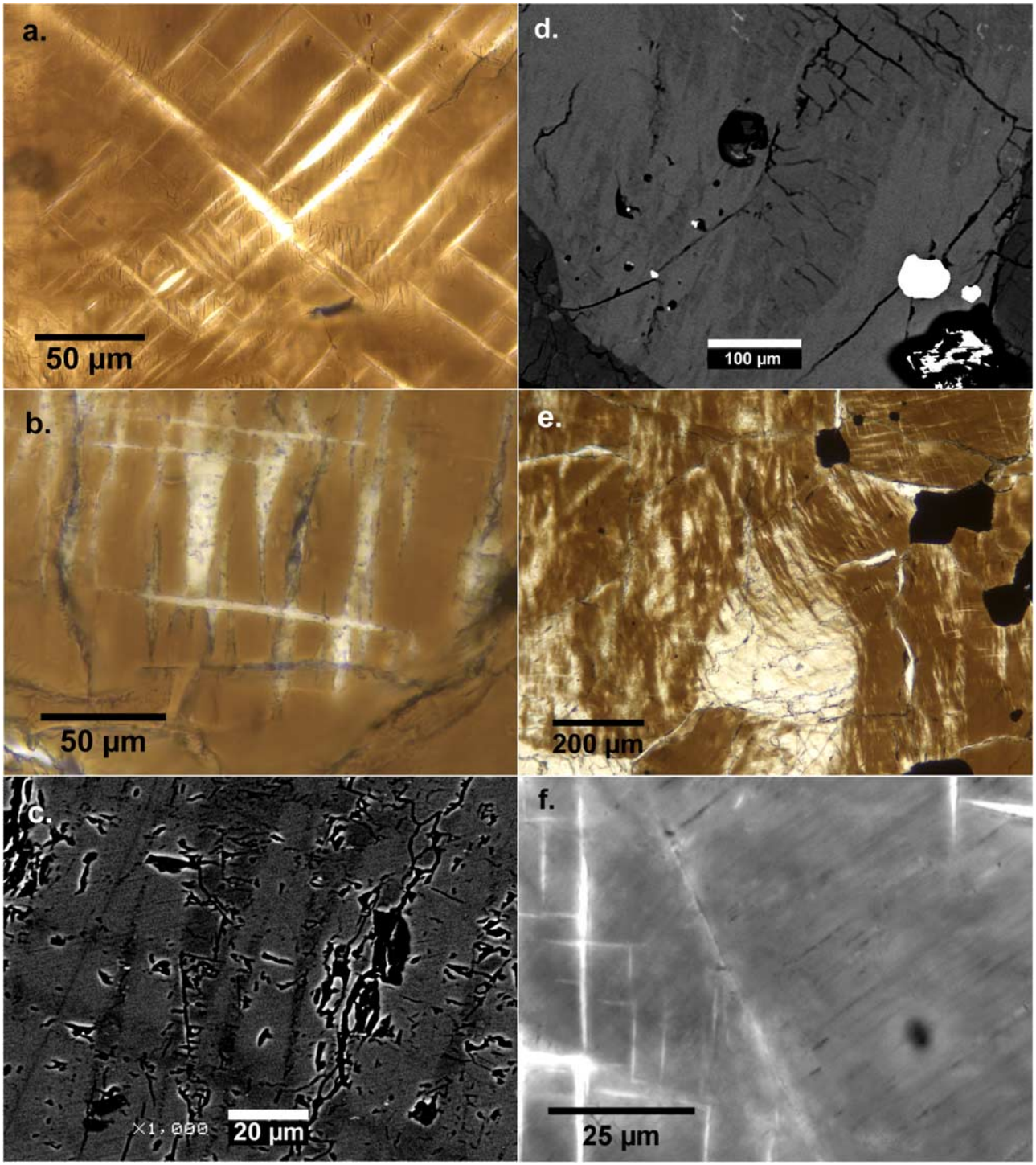

Figure 2

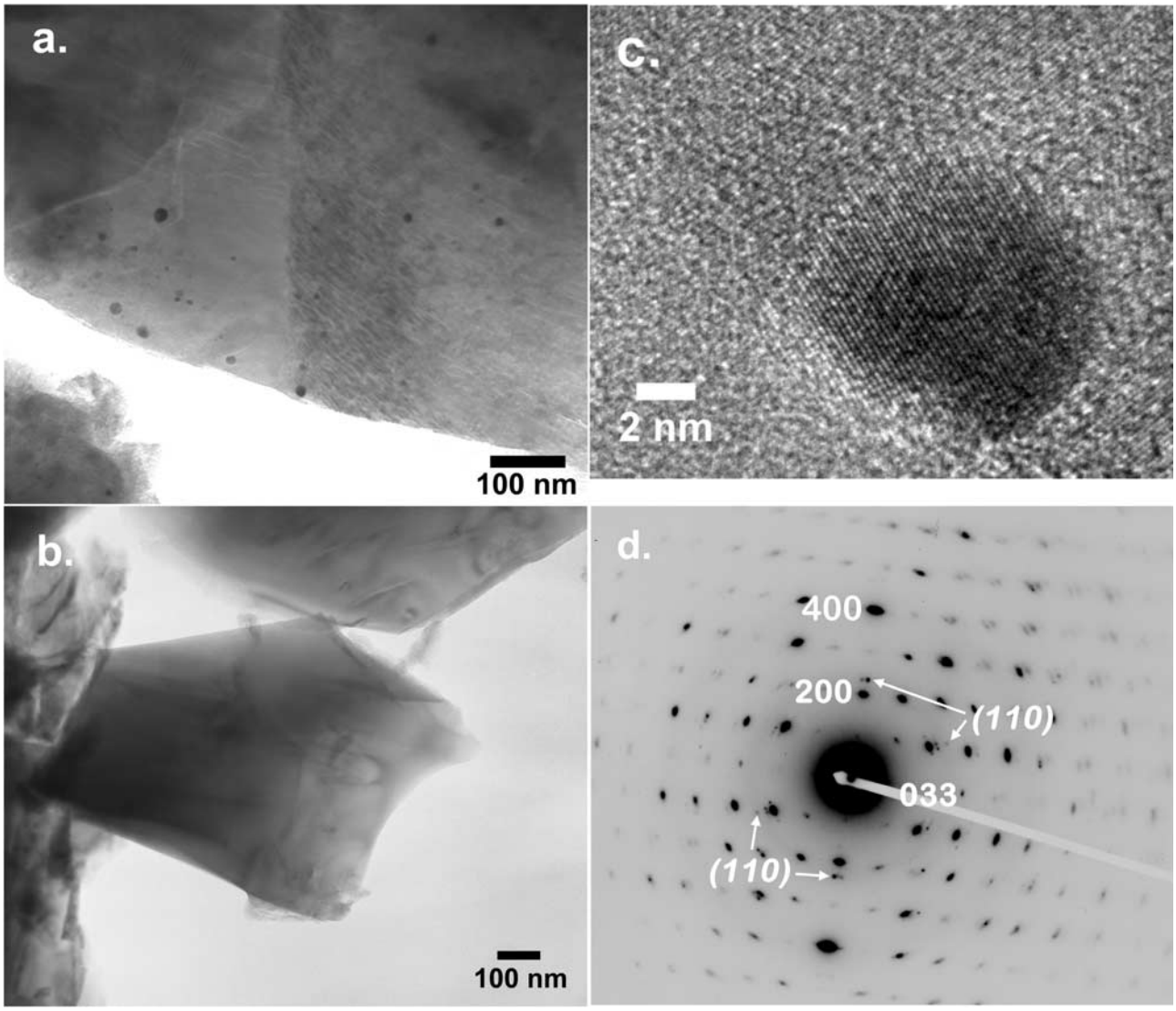

Figure 3. Transmission electron microscope images of olivine. Crushed grains mounted on holey carbon film. (a) Bright-field image, scale bar 200 nm. Olivine with small dark (electron-dense) spherules, patchy strain contrast, and multiple subgrains. Interpreted as visually brown (VB) olivine. (b) Bright-field image, scale bar 200 nm. Olivine without electron-dense spherules, and lacking significant strain contrast and subgrains. Interpreted as visually colorless (VC) olivine. (c) High-resolution bright-field image showing an electron-dense spherule (darker, center) like that of Figure 1a. Lattice fringes in spherule are at 0.2024 nm, consistent with [110] planes of iron-rich metal (kamacite). (d) Selected area diffraction image of VB olivine. Nonitalic indices are for olivine and refer to the diffraction spots just right of the index number. Electron beam down the [0−11] zone axis (space group Pbnm). Pattern yields a = 0.477 nm. Olivine diffractions show arcs concentric about origin, implying the presence of multiple subgrains. Many diffractions are doubled in the [011] direction, suggesting two phases of slightly different lattice parameters. Diffractions labeled (110) in italics have d = 0.2024 nm, consistent with (110) of α iron (kamacite).

EMP analysis of Fo_{78} (Table 2). Many diffraction spots in the VB olivine are doubled in the olivine (011) direction (Figure 3b). The olivine has d(011) = 0.54 nm, while the doubled spots show d ≈ 0.50 nm.

[23] The rounded inclusions are Fe-Ni metal [*Reynard et al.*, 2006a], as shown by EDS spectra and electron diffraction patterns consistent with a body-centered cubic lattice of α-Fe (Figure 3d): the [110] lattice spacing in 0.2024 nm. The Fe-Ni metal globules can be crystallographically aligned with their host olivine, with a [110] of the metal parallel to [100] or [122] of the olivine (Figure 3d).

3.1.2. Visually Colorless (VC) Olivine

[24] In grains with crystallographic a axes perpendicular to the thin section plane, colorless olivine appears as two sets of lenses, nearly at right angles to each other and symmetric with respect to the grains' optical extinction directions (Figure 2a). This orientation suggests that the colorless lenses are oriented approximately along {021}

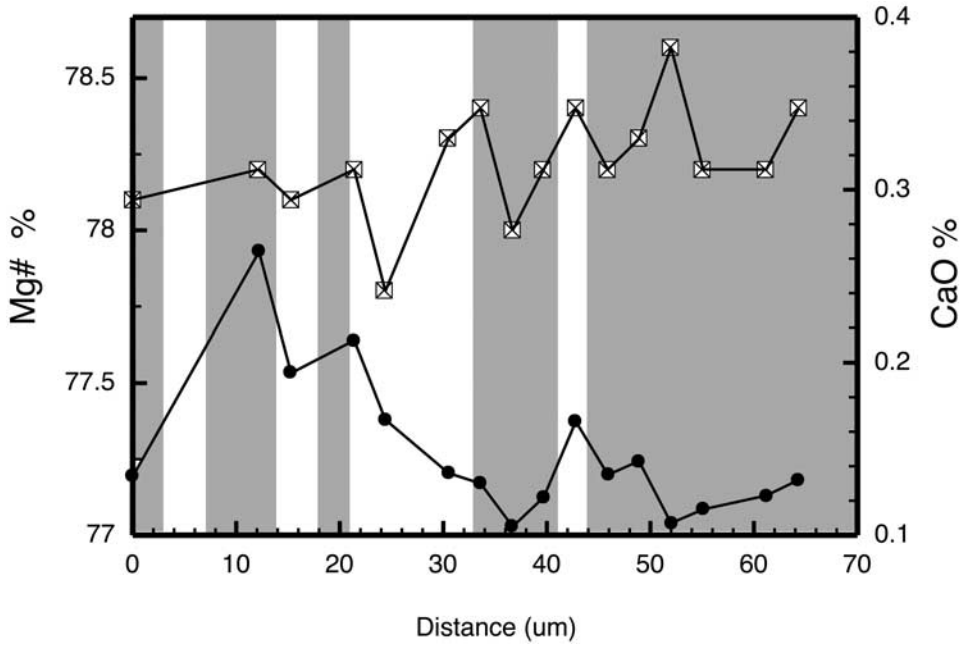

Figure 4. Chemical zoning profile across olivine grain of Figure 2c; see also Figures 2b and 1a. Zero distance here is the right end of line in Figure 2c. Mg# as squares, CaO content as filled circles. The traverse includes brown (VB) and colorless (VC) olivine, shaded and unshaded, respectively, on graph. The VB and VC olivine have the same Mg#, CaO content, and analytical totals (not shown).

planes. In grains with crystallographic a axes in (or near) the plane of the section, one sees anastomosing bands or flame-shaped patches of colorless olivine traversing the brown olivine (Figures 2b and 2c). Therefore the three-dimensional shapes of colorless olivine areas are interpenetrating and anastomosing ribbons, with long axes along a ([100]) and with short and intermediate axes near {021} planes. If a {021} plane of an olivine is near that of the thin section, the olivine can appear to be all colorless or all brown (Figures 2d and 2e). The elongations of colorless olivine ribbons are almost always parallel to the grains' a axes, but deviate strongly in rare grains. For example, flame-shaped patches of brown olivine in Figure 2e cross boundaries of olivine grains, and curve widely away from crystallographic directions.

[25] The visually colorless olivine commonly contains opaque micron-scale specks (Figure 2b), which are concentrated at its boundaries with brown olivine. These opaques appear infrequently at the thin section surfaces, and (by reflectance) may be Fe-Ni metal (like the inclusion) or spinel (magnetite or chromite).

[26] The colorless olivine is extensively cracked, predominantly near {100} and {010} planes (perpendicular to the a and b axes), which cross at right angles in appropriately oriented grains. Unlike the planar features in VB olivine, cracks in VC olivine are more widely spaced ($\sim$100 μm vs. $\sim$10 μm in VB), are long (in excess of a few hundred μm), are found in nearly all grains, and typically traverse an entire VC area. These cracks die out at the boundaries with VB olivine. The VC olivine rarely goes to optical extinction cleanly, so is apparently composed of subgrains like the VB olivine. However, the VC subgrains are larger than in the VB.

[27] Visually colorless olivine was apparently seen in TEM as a few grains in the mount, These did not show the mottling of strain contrast or the subgrains of the VB olivine, nor did they contain nanophase inclusions of iron metal (Figure 3b). Electron diffraction of these grains give a = 0.477 nm, as in the VB olivine.

3.1.3. Chemistry

[28] The olivine in NWA 2737 is chemically homogeneous. The average Mg#, molar Mg/(Mg + Fe) ratio, for 129 superior analyses (see above) is 78.3 ± 0.4% 2σ (Table 2), an analytical dispersion similar to that of the EMP standard. The Fe/Mn ratio is 49, consistent with that of olivines from other Martian meteorites [*Karner et al.*, 2003]. We found no significant chemical differences between brown olivine and colorless olivine (Figure 4) by EMP, including in abundances of Mg, Fe, Mn, Ca, and Al.

[29] The ferric iron content of the olivine is an important factor in understanding its unusual color. The three available constraints (EMP analyses, Mössbauer spectroscopy, and synchrotron micro-XANES) all suggest a low ferric iron content. The average of superior EMP analyses of olivine nominally implies that 0.7% of its iron is Fe^{3+} (Table 2). However, given the uncertainties in EMP analyses and standards, this value is consistent with no Fe^{3+}. Mössbauer spectra (Figure 5), described below, imply that the olivine has Fe^{3+}/Fe(total) < 3%, and which is consistent with no Fe^{3+} at all. SmX spectra are effectively identical for visually brown and colorless olivine (Figure 6), and show a pre-edge feature that could be a positive detection of Fe^{3+}. The positions of those features indicate Fe^{3+} at 14 ± 12% of total iron, with the imprecision arising because the centroids of the pre-edge peaks are poorly defined, and because they are in different positions on different spectra. This imprecision may be caused by the presence of Fe metal blebs in the olivine. The main FeK absorption edge for iron metal, at 7110 eV, is in the region of the olivine Fe^{3+} pre-edge peaks.

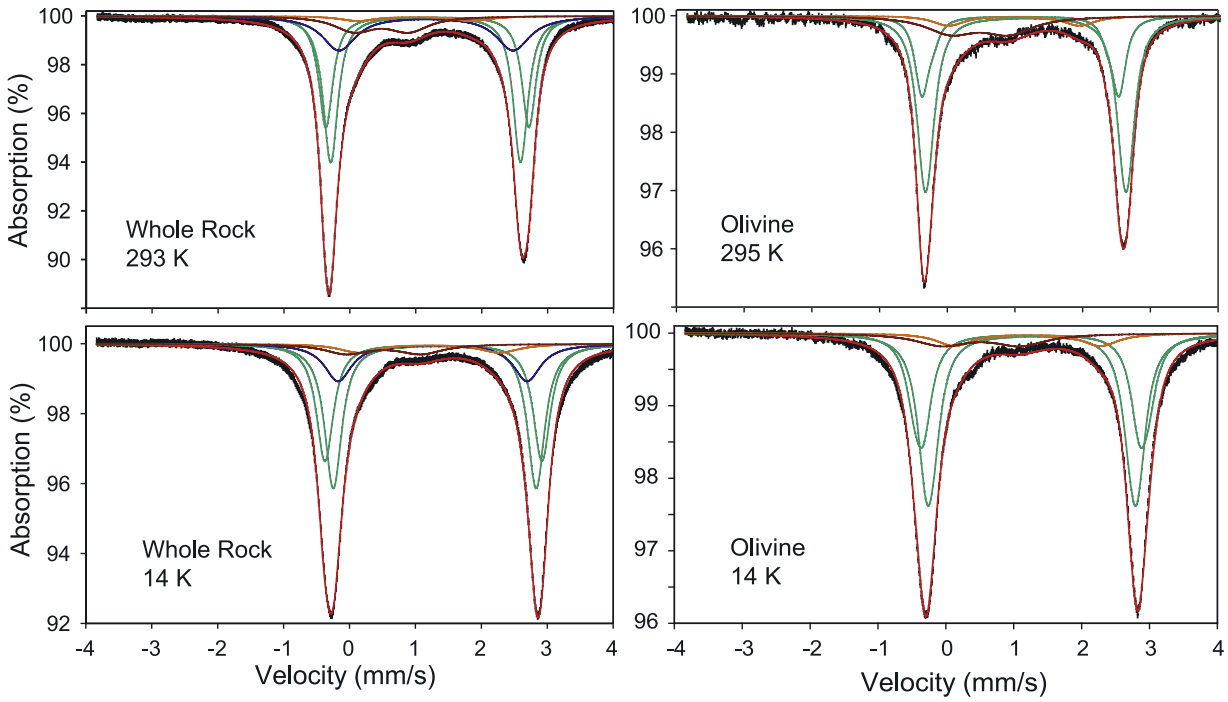

Figure 5. Mössbauer spectra of NWA 2737 whole rock and olivine separates from NWA 2737 at room temperature and liquid helium temperature (black bars) and deconvolution. Spectra are dominated by doublets for octahedrally coordinated Fe^{2+} in olivine (green). Other assignments are doublets for octahedrally coordinated Fe^{2+} in pyroxenes (blue), tetrahedrally coordinated Fe^{2+} in chromite (orange), and octahedrally coordinated Fe^{3+} in several minerals (maroon). The absence of peaks between −1 and −4 mm/sec imply that no sample contains a magnetically ordered phase (e.g., metal, magnetite, and pyrrhotite) at the 1% level. The red line represents the sum of all the component curves.

So, an olivine with iron metal and Fe^{3+} will show a misshapen and possibly misplaced pre-edge feature [*Delaney et al.*, 1996]. Thus these three methods are consistent with a low proportion of Fe^{3+} in the olivine, greater than 0% as suggested by SmX and less than 3% as required by Mössbauer. EMP data suggest Fe^{3+} closer to 0%, but are imprecise.

3.2. Pyroxenes

[30] Most areas among olivine grains of NWA 2737 are filled with complex intergrowths of high- and low-calcium pyroxenes (Figures 1d and 1e; *Beck et al.* [2006]). The high-calcium pyroxene is augite, average of $Wo_{39}En_{51}Fs_{10}$, (taking all iron as Fe^{2+}; Table 2). EMP analysis of the augite suggests that ∼15% of its iron is Fe^{3+}, which is consistent with Mössbauer (see below) and SmX data. The augite commonly contains fine-scale exsolution lamellae of low-Ca pyroxene (Figure 1e). The low-calcium pyroxene averages around Wo_{05}, but that value appears to be an average of two distinct populations (Table 2), averaging $Wo_{04}En_{77}Fs_{19}$, and $Wo_{06}En_{75}Fs_{19}$, labeled OPX and pigeonite respectively in Table 2. The crystal structures of these pyroxenes are not known.

3.3. Chromite

[31] Chromite is the dominant opaque mineral in NWA 2737, occurring as discrete crystals among olivine grains (Figure 1a) and as inclusions in olivine crystals (Figures 1f and 2d). The chromite grains among the olivine tend to have subhedral shapes, but are more euhedral when they abut mesostasis or pyroxene (Figure 1a, top left). Chromite inclusions in olivine grains are commonly euhedral to rounded, and range from 5 to ∼100 μm across. The few analyzed here span a moderate compositional range, with increasing Ti and Al offset by decreasing Cr (Table 2; see *Beck et al.* [2006]). Chromite inclusions in olivine tend to have lower Cr, while discrete grains are zoned from higher-Cr cores to lower-Cr rims. By EMP analyses, the chromites contain ∼12% of their iron as Fe^{3+} (Table 2). Chromite is dominantly a "normal" spinel, with its trivalent cations in the octahedral B sites (AB_2O_4), so the average NWA 2737 chromite formula can be cast as $(Fe^{2+}_{0.70}Mg_{0.29}Mn_{0.01})(Fe^{2+}_{0.05}Ti_{0.05}Fe^{3+}_{0.10}Al_{0.34}Cr_{1.46})O_4$. Note that nearly all of the Fe^{2+} is assigned to the tetrahedral site, consistent with the Mössbauer peak assignments (Figure 5).

3.4. Mesostasis

[32] Among the olivine and pyroxene grains is mesostasis material, characterized by abundant colorless silicate glass (optically isotropic), with lesser olivine and low-Ca pyroxene. Two types of silicate glass are present: "anorthoclase", with the chemical composition (but not crystal structure) of alkali feldspar (Table 2), and "granitic", with compositions like a mixture of silica and alkali feldspar [*Beck et al.*, 2006]. Orthopyroxene in the mesostasis is identical to the intercumulus grains in Mg# and Ti content, with slightly lower Ca and Al contents. The mesostasis hosts most of the minor minerals in NWA 2737, including chlorapatite,

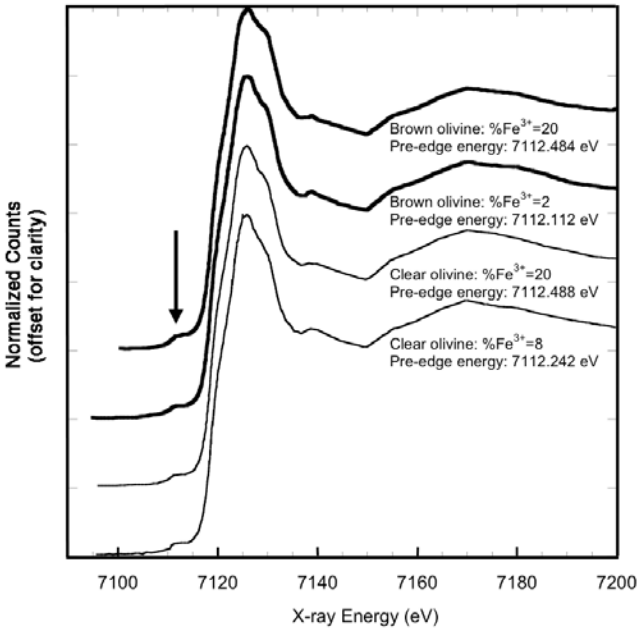

Figure 6. Synchrotron micro-XANES spectra of olivine, showing their FeK absorption edge (large peak) and pre-edge features (arrow). Spectra are offset for clarity. Visually brown (VB) olivine in heavy lines, visually colorless (VC) olivine in light lines. The energy centroid of the pre-edge feature reflects the proportion of Fe^{3+} in the olivine (both shown in Figure 6 for each spectrum). The pre-edge feature is affected by both crystal orientation effects and the presence of nanophase Fe metal, which lead to large uncertainties in Fe^{3+} measurement for these samples.

ilmenite, iron monosulfide (likely pyrrhotite), and probably rutile (small dark needles of very high birefringence). The presence of rutile is also consistent with an EMP analysis of a mesostasis spot with 9.6% TiO_2 and 3.0% FeO (in addition to Na, K, and Si consistent with anorthoclase glass, and Mg consistent with minor pyroxene). *Mikouchi et al.* [2005] report kaersutite amphibole in the mesostasis, but we did not locate any.

[33] Two types of mesostasis, structured and chaotic, were recognized. In structured mesostasis (Figure 1c), the anorthoclase-composition glass ($An_{04}Ab_{78}Or_{18}$, Table 3) has angular or rectangular edges when in contact with pyroxenes and other minerals, and forms elongated rectangles with their long axes nearly perpendicular to the edges of the mesostasis area (Figure 1c). These rectangles are exactly the shapes of anorthoclase crystals grown from magma. This texture is similar to that of mesostasis in the nakhlite meteorites where the elongated rectangles are albitic plagioclase [*Treiman*, 2005]. In chaotic mesostasis, "granitic" glass does not have regular boundaries against the other minerals. Rather, the pyroxenes and others minerals are angular fragments dispersed in the glass.

3.5. Magmatic Inclusions

[34] The olivine grains in NWA 2737 contain magmatic inclusions (Figures 1b and 2d), ellipsoidal bodies composed of several phases, including: "granitic" glass, aluminous augite, aluminous orthopyroxene, chromite, amphibole, iron sulfide, and chlorapatite (Table 3). Augite and orthopyroxene in inclusions have essentially the same Mg# as those among olivine grains, but have distinctly greater abundances of Al, Ti, and Na. The amphibole is brown, similar in color to the brown host olivine, and slightly pleochroic. Chemically, it is a kaersutite (Table 3), a calcic amphibole rich in titanium and alkalis. The Cl and F contents of the amphibole are low. We do not have analyses for OH in the amphibole, but SmX data suggest a significant proportion of its iron is Fe^{3+}, and the chemical formula suggests a significant substitution of O^{2-} in place of OH (Table 3).

[35] The largest magmatic inclusions, to 150 μm across, are texturally similar to those in Chassigny [*Floran et al.*, 1978; *Johnson et al.*, 1991] in that they contain blocky crystals of pyroxene and amphibole set in "granitic" glass (Figure 1b). In some, pyroxene crystals are arranged as if they grew inward from the walls, comparable to (but coarser than) textures of magmatic inclusions in the Nakhla Martian meteorite [*Treiman*, 1993]. Commonly, glass patches in the inclusions are surrounded by void space (now filled with epoxy). The glass has scalloped and irregular edges against the void space, while the silicate minerals maintain straight, crystallographically controlled boundaries.

[36] Smaller magmatic inclusions range down to a few tens of micrometers in diameter. They consist mostly of silicate glass and chromite in highly variable proportions.

3.6. Alteration

[37] The NWA 2737 meteorite shows little evidence of low-temperature alteration, either terrestrial or Martian. Rare orange patches apparently represent rust minerals (Fe^{3+} oxyhydroxides) deposited on fractures. By analogy with other weathered meteorites, these patches could represent former locations of sulfide minerals: We suspect that the rusts are terrestrial, but lack stratigraphic markers for their age. Fractures and grain boundaries commonly are filled with films or veins of magnesian calcite (Figures 1e and 1f). We have not found textural evidence to show whether this carbonate is terrestrial or Martian. It seems likely to be terrestrial, given that the Rb-Sr radio-isotope system is disrupted by addition of a component with a high initial Sr ratio, like desert soil carbonate [*Misawa et al.*, 2005a].

[38] Finally, some of the feldspathic glasses in the mesostasis and in magmatic inclusions show signs of dissolution. The edges of these glass pools are serrated and scalloped and are separated from nearby silicate and oxide minerals by void spaces (in thin section, filled with epoxy glue). Nearby olivine shows no sign of dissolution.

4. Mössbauer Spectroscopy

[39] Two different samples were analyzed using Mössbauer spectroscopy: the olivine separate and the whole rock (Table 4 and Figure 5). Each was run at 293 K and at 12 K or 14 K. All the spectra are quite similar except for the expected peak shifts at low temperature: Both isomer shift and quadrupole splitting increase as temperature decreases. Broadly, the spectra are dominated by ferrous iron in olivine. There are small contributions from ferrous iron in pyroxene and chromite, and a small proportion of ferric iron recognizable in all spectra.

Table 4. Mössbauer Spectrometry Results

		Whole Rock		Olivine	
Assignment	Parameter[a]	293 K	14 K	293 K	14 K
Fe^{2+} olivine	Δ, mm/s	1.18	1.27	1.08	1.26
	Δ, mm/s	3.07	3.31	2.91	3.18
	Γ, mm/s	0.25	0.30	0.21	0.30
	% Area	28	32	23	34
Fe^{2+} olivine	δ, mm/s	1.15	1.29	1.16	1.27
	Δ, mm/s	2.84	3.08	2.98	3.10
	Γ, mm/s	0.25	0.30	0.26	0.30
	% Area	38	39	55	49
Fe^{2+} pyroxene	δ, mm/s	1.16	1.26		
	Δ, mm/s	2.64	2.87		
	Γ, mm/s	0.62	0.50		
	% Area	21	16		
$^{[T]}Fe^{2+}$ chromite	δ, mm/s	0.99	1.21	0.99	1.20
	Δ, mm/s	1.72	2.16	1.97	2.18
	Γ, mm/s	0.66	0.70	0.52	0.62
	% Area	3	6	6	7
$^{[M]}Fe^{3+}$ olivine, chromite	δ, mm/s	0.48	0.52	0.48	0.52
	Δ, mm/s	0.82	1.19	0.84	1.18
	Γ, mm/s	0.67	0.80	0.88	0.92
	% Area	10	7	15	9
	χ^2	7.33	20.4	1.18	5.14

[a]Δ is quadrupole splitting, δ is isomer shift, and Γ is peak width at half maximum. % Area is the percentage of the integrated area under the Mössbauer spectrum assigned to a doublet: It is equal to the atomic % iron in the sample assigned to that doublet. χ^2 is a statistical measure of the quality of the fit: Lower values are better fits.

4.1. Mössbauer Spectra and Peak Assignments

[40] The Mössbauer spectra of the NWA 2737 bulk rock and the olivine separate are dominated by olivine. The spectra are fit by two doublets with IS and QS reasonable for $^{[M]}Fe^{2+}$ in olivine (Table 4 and Figure 6). The 293 K spectra are fit well with two doublets of subequal areas with IS = 1.13 ± 0.05 mm/sec, and the 14 K spectra are fit similarly by two doublets with IS near 1.27 mm/sec.

[41] In the whole rock spectra, another $^{[M]}Fe^{2+}$ doublet is assigned to M1 sites in pyroxene on the basis of its parameters, the 12 K spectrum of IS = ~1.26 mm/s, QS = ~2.37 mm/s [e.g., *Dyar et al.*, 1989]. The area of that doublet, 16–21% of the total iron, is higher than expected for pyroxene from the modal analysis (Table 1), but generally consistent if the bulk sample had more pyroxene than the analyzed thin section. This Fe^{2+} doublet is relatively broad (0.62 mm/s in the 293K data), which could reflect the presence of three species of pyroxene (augite, orthopyroxene, and pigeonite) in the sample (Table 1). We did not detect the second doublet that arises from Fe^{2+} in the pyroxene M2 site (QS = ~2.00 mm/s), probably because augite is the dominant pyroxene in NWA 2737 (Table 1), and because augite has little Fe^{2+} in its M2 site.

[42] The remaining peaks in the Mössbauer spectra are small, overlapped by the olivine and pyroxene doublets, and admit several possible interpretations. The peaks and shoulders in question are: [1] δ = 0.99 mm/s in the 293 K spectra and ~IS = 1.20 mm/s in the 13 K spectra; and [2] at δ ≈ 0.50 mm/s in all spectra (Figure 5).

[43] The first of these doublets has parameters corresponding to Fe^{2+} in tetrahedral coordination, and we assign it to chromite [e.g., *Osborne et al.*, 1981; *Chen et al.*, 1992]. Work by *Li et al.* [2002] on natural chromite reported three doublets with 298K parameters of δ = 0.97, 0.97, and 0.39 mm/s and Δ = 1.56, 0.90, and 0.56 mm/s respectively. The first of these doublets is a good match to our doublet with δ = 0.99 mm/s and Δ = 1.72 and 1.97 mm/s in the spectra of the whole rock and olivine "separate", respectively. Differences between the values reported in *Li et al.* [2002] and our own data can be attributed to temperature differences between their study and ours, and to the small amount of chromite in our sample, which makes its peaks difficult to resolve from others peaks.

[44] The 14 K spectrum of the bulk rock can be fit with a doublet at δ = 1.20–1.21 mm/s and Δ = 2.16–2.18 mm/s. In comparison, *Li et al.* [2002] reported 90 K parameters for chromite of δ = 1.11, 1.15, and 0.43 mm/s and Δ = 2.82, 1.86, and 0.81 mm/s respectively. These results suggest that at low temperatures, the first chromite doublet may well be indistinguishable from the olivine doublets; in fact, we do not see any detectable increase in the area of either of the olivine doublets at low temperatures. Alternatively, our single low-temperature doublet assigned to chromite may represent a composite of unresolved small contributions from the subcomponents of the tetrahedral chromite doublets.

[45] Another possible assignment of the δ = 0.99 mm/s doublets might be to wadsleyite, the high-pressure polymorph of olivine in a modified spinel structure, which was suggested to be present in NWA 2737 olivine by *Reynard et al.* [2006a]. However, the Mössbauer spectra of iron-bearing wadsleyite have δ = 1.05 mm/s and Δ = 2.8 mm/s [*O'Neill et al.*, 1993], very similar to olivine itself (Figure 5 and Table 4).

[46] The smaller δ doublet is the most important in understanding the oxygen fugacity under which this meteorite equilibrated; unfortunately, it is the most difficult to interpret uniquely. The parameters are typical of those for six-coordinated Fe^{3+} in a wide variety of host minerals including olivine, pyroxene, or oxide because the range of IS and QS for $^{M}Fe^{3+}$ is quite small. This doublet is small and poorly resolved, with an area of 7–15% of the total Fe in the samples. The parameters of this doublet in our spectra (δ = 0.48 and 0.52 mm/s and Δ = 0.82–0.84 and 1.18–1.19 mm/s at 293 and 14 K, respectively) are somewhat higher than those for chromite as noted above, favoring the interpretation that the Fe^{3+} is in a silicate. Because this doublet is present in the olivine "separate" that has no features associated with Fe^{2+} in pyroxene, the most likely assignment is to Fe^{3+} in olivine (and included chromite). By way of comparison, *Banfield et al.* [1992] reported parameters of δ = 0.45 mm/s and Δ = 0.52–0.73 mm/s for Fe^{3+} in oxidized olivine, fairly close to our parameters within ±0.05 mm/s error bars.

[47] Finally, we note that there is no evidence that NWA 2737 contains a magnetically ordered phase (iron metal, magnetite, hematite, or pyrrhotite) at the level of 1% of total Fe. These phases would show absorption feature between −4 to −1 mm/s, and none are seen in any spectrum (Figure 5).

4.2. Iron Distribution

[48] For comparison with Mössbauer spectra, we calculate the distribution of iron among the minerals of NWA 2737 from the EMP results. The average olivine here (Table 2) has 0.43 moles Fe^{2+} per molar formula unit

M_2SiO_4 of ~44.3 cm^3/mol, giving 0.0097 mole-Fe^{2+}/cm^3. The average pyroxene here (taking the modal proportions of augite and orthopyroxene from Table 1 and the analyses of Table 2) has 0.25 moles Fe^{2+} and 0.024 moles Fe^{3+} per formula unit $M_2Si_2O_6$, in an estimated volume of ~64.6 cm^3/mol, giving 0.0039 mole-Fe^{2+}/cm^3 and 0.0004 mole-Fe^{3+}/cm^3. The average chromite has 0.693 moles Fe^{2+} and 0.115 moles Fe^{3+} per formula unit AB_2O_4 of ~44.0 cm^3/mol, giving 0.0158 mole-Fe^{2+}/cm^3 and 0.0026 mole-Fe^{3+}/cm^3.

[49] Combining these data with the mineral volume proportions of Table 1, one derives the distribution of iron among the minerals in NWA 2737. Of the iron in NWA 2737, EMP data imply that 99% of the Fe is ferrous, and 91% of that is in olivine. Thus EMP data imply that 90% of the iron in the meteorite is Fe^{2+} in olivine, compared to a value of 71% from Mössbauer (using the 14 K bulk rock spectrum). Three fourths of the remaining ferrous iron is in pyroxene and one fourth in chromite (again using the 14 K bulk rock spectrum). EMP data suggest that 1% of the iron in NWA 2737 is Fe^{3+}, while the Mössbauer bulk spectrum gives ~7%.

[50] For determining the oxidation state of NWA 2737, it is important to understand how the ferric iron in distributed among its phases, especially whether we can constrain the Fe^{3+} content of the olivine. Unfortunately, the Mössbauer spectra are not readily interpreted in terms of Fe^{3+} in olivine. The olivine separate contains some chromite, which is the source of the doublet assigned to $^{T}Fe^{2+}$. The $^{[M]}Fe^{3+}$ doublet in that spectra, 9% of the total Fe (14 K olivine separate spectrum), includes ferric iron in both olivine and chromite. From EMP data (Table 2), $^{[M]}Fe^{3+}$ in chromite is ~0.1 of $^{[T]}Fe^{2+}$; whereas the Mössbauer spectra imply subequal proportions. However, considering the uncertainties in ascribing peaks to chromite, we conclude only that <3% of the iron in olivine is Fe^{3+}.

5. Synchrotron Micro-Xanes Spectroscopy

[51] Synchrotron micro-XANES spectroscopy (SmX) has significant potential for determining the oxidation states of iron in areas as small as tens of microns across in thin section [*McCanta et al.*, 2004a]. This determination comes from the location of the pre-main-edge absorption feature; its energy is systematically related to the Fe^{3+}/Fe^{2+} ratio of the target material [*Wilke et al.*, 2001; *Mottana et al.*, 2002; *Dyar et al.*, 2002].

[52] Although SmX works well in many types of samples, it yields imprecise and contradictory results for olivine in NWA 2737 – Fe^{3+} contents from a few percent to twenty percent of total iron on seemingly identical areas (Figure 6). Three factors may be in play here: low Fe^{3+} contents, orientation effects, and presence of Fe metal. Olivine in NWA 2737 is expected to have relatively little Fe^{3+}, at least on the basis of its oxidation state and comparison with terrestrial samples (see above). Unfortunately, SmX is least precise for low Fe^{3+} contents [*McCanta et al.*, 2004a]. XANES and SmX measurements are sensitive to crystal orientation [*Dyar et al.*, 2002], although the extent of anisotropy in olivine is not known. Finally, the VB olivine contains nanophase iron metal, which is a problem because the main Fe absorption edge of iron metal overlaps the pre-edge features of iron in oxygen environments [*Delaney et al.*, 1996; *McCanta et al.*, 2004a].

[53] So SmX data are consistent with the olivine containing relatively little Fe^{3+}, nominally 14 ± 12%, but cannot be considered quantitative at this time. It will be worth investigating these olivines further with SmX and EELS, with careful control on crystal orientation.

6. Geologic History

[54] A major purpose of this work is to relate the geological history of NWA 2737 to its EM spectroscopic signature, so that the signature (i.e., that of VB olivine) can be used to help interpret remotely sensed spectra of Mars. The petrography and mineral chemistry of NWA 2737 outline this history: formation as an olivine-rich cumulate rock from a basaltic magma, complete or partial equilibration of its mineral compositions (probably in postigneous cooling), a major shock metamorphism and deformation (probably at 170 Ma), and a second shock deformation (possibly at ejection from Mars). There is no certain evidence of aqueous alteration on Mars, and only limited alteration on Earth.

6.1. Igneous: Liquidus to Solidus

[55] From its mineralogy, mineral compositions, and textures, it is clear that NWA 2737 formed from basaltic magma; that is, it is an igneous rock comparable to Chassigny [*Floran et al.*, 1978; *Johnson et al.*, 1991; *Wadhwa and Crozaz*, 1995]. Like Chassigny, it contains olivine in far greater abundance than typical magmas, and so is inferred to be enriched in olivine relative to its parent magma; that is, it is a cumulate igneous rock. Within its olivine crystals are magmatic inclusions like those in other Martian igneous rocks [e.g., *Treiman*, 2005]. The feldspar-rich mesostasis in NWA 2737 is texturally like rapidly quenched basaltic magma [*Treiman*, 2005].

[56] The parent magma of NWA 2737 was strongly enriched in incompatible elements [*Beck et al.*, 2006], as was the parent of Chassigny. The parent magma composition was certainly basaltic, in a broad sense, with a low-pressure liquidus temperature of ~1150–1200°C or so. The exact composition of the chassignites' parent magmas is a matter of dispute, especially their abundances of alkali elements [*Longhi and Pan*, 1989; *Johnson et al.*, 1991; *Filiberto and Nekvasil*, 2006].

[57] The mesostasis shows igneous textures typical of rapidly cooled feldspathic magma: elongated discrete laths of feldspar (Figure 1c; now diaplectic glass). Suitable experiments on this mesostasis composition could probably constrain its cooling rate or degree of undercooling, as was done for plagioclase by *Grove* [1978]. The presence of a single ternary feldspar implies crystallization above the alkali feldspar solvus; for the average mesostasis feldspar ($An_{08}Ab_{74}Or_{18}$; *Beck et al.* [2006]) this implies crystallization at or above ~800°C [*Wen and Nekvasil*, 1994].

6.2. Near-Solidus/Subsolidus Processes

[58] The mineral chemistry of NWA 2737 suggests extensive metamorphism (subsolidus chemical equilibration), and the conditions of this metamorphism are important for understanding its spectroscopic characteristics.

Minerals in NWA 2737 do not retain typical igneous zoning patterns (e.g., magnesian core compositions, oscillatory zoning), but are chemically homogeneous (olivine, feldspar, each pyroxene species) or nearly so (chromite). This homogeneity in an igneous rock implies diffusional equilibration, and an approach to subsolidus chemical equilibrium. For simplicity, we interpret this equilibration to represent slow cooling of an igneous body after emplacement, but it could represent a later thermal event.

6.2.1. Temperature

[59] Two relatively precise mineral thermometers are accessible in NWA 2737: Ca-Fe-Mg distribution between orthopyroxene and augite and Fe-Mg distribution between chromite and olivine. The two-pyroxene thermometer is appropriate because low-Ca and high-Ca pyroxenes are distinct, coexisting, and homogeneous. Using the calibration of QUILF [*Andersen et al.*, 1993], the average pyroxene compositions imply equilibration at ~1150°C (Table 2), and the most calcic augite and least calcic orthopyroxene give ~1100°C. Independently, *Reynard et al.* [2006a] have derived similar temperatures. For comparison, Chassigny pyroxenes give ~1100–1150°C [*Johnson et al.*, 1991; *Wadhwa and Crozaz*, 1995]. These temperatures are near the solidus of basalt, and so suggest that NWA 2737 spent enough time at or near its solidus to permit equilibration of its pyroxenes.

[60] Olivine-spinel equilibration temperatures, calculated with the MELTS supplemental calculator [*Sack and Ghiorso*, 1991a, 1991b], are ~800°C and ~825°C for chromites 1 and 2 (Table 2). With the same calibration, olivine-spinel in Chassigny gives equilibration at ~850°C (data of *Floran et al.* [1978]). These temperatures are lower than those from two-pyroxene thermometry, because Fe-Mg diffusion in these phases is much more rapid than Ca diffusion in pyroxenes [see *Treiman*, 1995]. This temperature most likely reflects blocking of Fe-Mg diffusion as a late igneous or postigneous processes, and is very similar to the minimum crystallization temperature of ~800°C for the mesostasis feldspar (see above, *Wen and Nekvasil* [1994]). It seems likely, then, that the Fe-Mg last equilibrated between olivine and spinel during solidus crystallization of the mesostasis.

6.2.2. Thermal History and Setting

[61] NWA 2737 was emplaced as an igneous cumulate rock at T > 1150°C, spent enough time near that temperature to exsolve and homogenize its pyroxenes, and then cooled rapidly enough through the solidus of the mesostasis (~800°C?) to produce its variolitic texture. This latter temperature was preserved in the olivine-spinel thermometer.

[62] This type of cooling history (slow at high temperature, fast at lower temperature) is not as expected from a point-shaped or planar thermal anomaly (like a thin lava flow) emplaced into a cooler medium [*Carslaw and Jaeger*, 1959], although previous models of chassignite cooling implicitly use point or plane geometries [*Monkawa et al.*, 2004; *Mikouchi et al.*, 2005; *Reynard et al.*, 2006b]. However, slow cooling at high temperature followed by faster cooling at low temperature is consistent with that of a rock mass in the interior of a larger partially molten body, like a sill or a package of hot flows [*Jaeger*, 1968]. Rock at the walls of a large mass cools rapidly; the interior remains hot because (1) it takes significant time for the "cold" of the walls to diffuse in and (2) temperature is buffered above and at the solidus by the heat released by crystallization. Thereafter, the body cools relatively rapidly by conduction. With thermal modeling, it may be possible to constrain the size of the magma body for NWA 2737, and its place in the body.

6.3. Oxidation State

[63] The oxidation state of NWA 2737 is important for understanding its spectral characteristics, because the oxidation state of iron strongly affects reflectance in the visible and near IR. The Martian meteorites formed across a large range of oxidation states [*Herd et al.*, 2001, 2002a, 2002b; *Goodrich et al.*, 2003; *Herd*, 2003, 2006; *McCanta et al.*, 2004b]. The most reduced meteorite is QUE 94201, which formed at an oxygen fugacity (f_{O2}) near the iron-wüstite buffer (~3.5 log units below the quartz-fayalite-magnetite (QFM) buffer. The most oxidized are the nakhlites, which formed at ~QFM − 1 to ~QFM + 1 [*Szymanski et al.*, 2003; *Dyar et al.*, 2005]. Chassigny, the meteorite most like NWA 2737, is also fairly oxidized at ~QFM − 1.25 (unpublished calculations), with higher f_{O2} in magmatic inclusions [*Delaney and Dyar*, 2001]. The oxidation state of NWA 2737 during metamorphism was QFM to QFM − 1, on the basis of mineral equilibria and ferric iron abundances.

6.3.1. Mineral Equilibria

[64] Potentially, the most useful oxybarometer for NWA 2737 is the olivine-pyroxene-spinel equilibrium $3\ Fe_2SiO_4(olivine) + \frac{1}{2}\ O_2 = Fe_3O_4(spinel) + 3\ FeSiO_3(pyroxene)$ [e.g., *Wood*, 1991; *Ballhaus et al.*, 1991]. *Herd et al.* [2002a, 2002b] and *Herd* [2003, 2006] applied this equilibrium in Martian basaltic and lherzolite meteorites, using temperatures from Fe-Mg distribution between olivine-spinel [*Sack and Ghiorso*, 1991a], and the activity of magnetite from the MELTS Supplemental Calculator [*Sack and Ghiorso*, 1991a, 1991b].

[65] However, this oxybarometer can only be applied if the pyroxene was in Fe-Mg equilibrium with the olivine and spinel at their equilibration temperature: 800–825°C. The only available test of this possible equilibrium is the distribution of Fe/Mg between olivine and orthopyroxene. This equilibrium is mostly independent of Ca distribution between the pyroxenes, basis for two-pyroxene thermometer (above), because Fe and Mg in pyroxene diffuse much more rapidly than does Ca. The experiments of *von Seckendorf and O'Neill* [1993] show that Fe/Mg distribution between olivine and orthopyroxene is essentially independent of temperature for compositions like those of NWA 2737, and the compositions of olivine and orthopyroxene in NWA 2737 (Table 2) are consistent with their experimental equilibria. Similarly, the QUILF calibration [*Andersen et al.*, 1993] gives an equilibration temperature of 540 ± 360°C for olivine and orthopyroxene, which is operationally an identical result to that from the experiments of *von Seckendorf and O'Neill* [1993]. So, one cannot show that the olivine, pyroxene, and chromite were in Fe-Mg disequilibrium near 800°C, and we may proceed with calculating an oxygen partial pressure.

[66] Applying the *Wood* [1991] thermo-oxybarometer to chromite 1 (adjacent to olivine, high Ti and Al, Table 2) yields $f_{O2} \sim$ QFM − 0.5 log units; applying it to chromite 2

yields $f_{O2} \sim$ QFM − 1.25. These values are uncertain to ~0.5 log units, and so are similar within uncertainty to each other and to Chassigny's oxidation state f_{O2} = QFM − 1.25 (method of *Wood* [1991]; mineral composition data from *Floran et al.* [1978] and *Wadhwa and Crozaz* [1995]); *Beck et al.* [2006] calculate a nearly identical value from the distribution of V among minerals.

6.3.2. Ferric Iron Abundance

[67] Independent of the above equilibria, a comparison of ferric iron abundances in NWA 2737 with those of terrestrial rocks also suggests an oxidation state near the QFM buffer. Typical mantle peridotite from the Earth equilibrated near QFM, and its augite and olivine generally contain Fe^{3+} as 10–20% and <1% respectively of their total Fe [*Dyar et al.*, 1989, 1992, 1996]. Metasomatized amphibole-bearing mantle rock equilibrated at more oxidizing conditions, ~QFM + 2, and its augite and olivine contain Fe^{3+} as ~30% and ~4% respectively of their total Fe [*Dyar et al.*, 1989, 1992, 1996; *McGuire et al.*, 1991]. These ranges for natural samples are consistent with laboratory experimental work [*McCanta et al.*, 2004b], in which augite equilibrated at ~QFM (~IW + 3.5) has ~12% of its iron as Fe^{3+}.

[68] As discussed above, augite and olivine in NWA 2737 contain Fe^{3+} as ~15% and 0–3% respectively of their total Fe (Table 4). These proportions of Fe^{3+} are like those in normal Earth mantle rocks, and so represent an oxidation state of ~QFM. NWA 2737 might be a bit more reducing than that, given the relatively low Fe^{3+} content of its pyroxenes and the range of Fe^{3+} in mantle augites. Given the uncertainties in these estimates, they are reasonably consistent with the mineral equilibria results of ~QFM – 1.

6.4. Major Shock Event

[69] Many features of NWA 2737 are products of strong shock, i.e. to shock stage S5 in the scheme of *Stöffler et al.* [1991] (amended by *Stöffler et al.* [1992], *Rubin et al.* [1997], *Schmitt* [2000]). These features include (1) transformation of feldspar to diaplectic glass, (2) localized melting, (3) planar deformation features in olivine, (4) the dark color of the olivine, (5) the fine-scale mosaicism of the olivine, (6) the partial transformation olivine to a denser polymorph, and (7) heat sufficient to reset the K-Ar chronometer [*Stöffler et al.*, 1991; *Bogard and Garrison*, 2006].

[70] Glasses of several sorts in NWA 2737 are ascribed to shock. The most obvious of them are the glass "pseudomorphs" after original crystals of alkali feldspar in the mesostasis (Figure 1c). This transformation, calibrated for oligoclase feldspar in chondrites, occurs at (and above) peak shock pressures of ~35 GPa and shock stage S5. Pockets of bulk shock melt can appear in stages S3 and above, and similar olivine-rich shock melts occur in Chassigny [*Melosh et al.*, 1983]. Areas of chaotic textured mesostasis are interpreted as melted and mobilized mesostasis material, and are also consistent with an overall shock stage of S5.

[71] The micron-scale discontinuous lamellae in the olivine on {010} and {001} planes (Figure 2f) are characteristic of, and interpreted as, planar deformation features (pdfs) [*Stöffler et al.*, 1991; *D. Stöffler*, personal communication, 2006]. They are produced typically in S5 and above, and rarely at S3–S4. Considering their abundance in NWA 2737 olivine, they indicate an overall shock stage of S5. As with other pdfs, they represent local frictional melting along preferred slip systems, here most likely [100]{010} [see *Cordier*, 2002]. This orientation has not been reported for exsolutions or intercalations of other phases, such as laihunite or humite-group minerals [e.g., *Kitamura et al.*, 1987; *Banfield et al.*, 1990, 1992; *Janney and Banfield*, 1998].

[72] The brown color of the olivine can arise from shock at stage ~S6, as in chondrites [*Stöffler et al.*, 1991], laboratory experiments [*Bauer*, 1979], and other Martian meteorites (ALHA77005 and LEW88516; *Ostertag et al.* [1984]; *Treiman et al.* [1994]). For his experimental conditions, *Bauer* [1979] showed an extended time at high temperature (not just the shock event) produced nanophase particles of magnetite in the olivine, and those produced the brown color. TEM observations show that the NWA 2737 olivine contains nanophase particles of iron metal, which are (in part) responsible for its color.

[73] The VB olivine is extensively mosaicized, i.e. converted to small domains or subgrains of slightly different orientations. This is seen optically as small domains with differing extinction positions (Figures 1d and 1f), in TEM bright-field imagery as blotchy tone (Figure 3a), and SAED as asterism around diffraction spots (Figure 3d; *Reynard et al.* [2006a]). This strong mosaicism arises at shock level S5 [*Stöffler et al.*, 1991].

[74] Also, *Reynard et al.* [2006a] report that VB olivine shows Raman scattering lines consistent with wadsleyite, a high-pressure polymorph of olivine in a modified spinel structure. The finding that VB olivine contains a phase like olivine but with a smaller unit cell (and the same chemical composition; Figure 3d) and the higher BSE brightness of VB olivine compared to VC (Figures 2c and 2d) are both consistent with the presence of a denser polymorph of olivine. The shock classification of *Stöffler et al.* [1991] does not include a transformation of olivine to wadsleyite, but does include transformation to the spinel-structured ringwoodite in shock stage S6. Thus it seems reasonable that formation of wadsleyite might represent a slightly lower pressure of shock stage S5–S6.

[75] These shock characteristics are all consistent with a shock event of S5–S6, suggestive of peak shock pressure of ~55 GPa [*Stöffler et al.*, 1991]. This would be a major shock event, and would leave the rock significantly hotter than it began. How much hotter is not obvious, as the equation of state for a rock like NWA 2737 (with a few percent alkali feldspar, Table 1) is not known. A pure dunite sample shocked to ~ 55 GPa would be heated by only a few hundred degrees C [*Fritz et al.*, 2005], while a chondrite might be heated 500°C or more [*Schmitt*, 2000]. The difference between the dunite and the chondrite arises because of porosity and impedance mismatch among minerals, and it seems reasonable that NWA 2737 would be intermediate between the dunite and the chondrite. In this case, heating of ~300–500°C would likely sufficient to degas much of the ^{40}Ar in the rock, and thus reset the Ar-Ar chronometer [*Stöffler et al.*, 1991; *Bogard and Garrison*, 2006].

[76] Also, such a significant time at elevated temperature is required for the formation of nanophase precipitates in the olivine. *Bauer* [1979] found that shock alone did not permit olivine to exsolve nanophase particles of magnetite, but that sustained postshock heating was required. NWA 2737 has

iron metal rather than magnetite, but the physical principles are, it seems to us, identical. To form either magnetite or iron metal in olivine, it must be hot enough for enough time to allow diffusion of Fe and O across hundreds of nanometers. It seems that this requirement is much less stringent than that of degassing ^{40}Ar [*Bogard and Garrison*, 2006] from the whole sample, so that formation of nanophase iron metal or magnetite should be seen as a logical consequence of postshock heating.

6.5. Deformation

[77] Most of the deformational features in NWA 2737 can be ascribed to shock, but the ribbons of visually colorless (VC) olivine (Figures 1 and 2) are not mentioned in guides to shock deformation of chondrites [*Stöffler et al.*, 1991, 1992; *Rubin et al.*, 1997]. These ribbons can be ascribed to postshock deformation and recrystallization of VB olivine, at high temperature and with strain rates more typical of tectonic deformation than shock. This inference about the VC olivine ribbons follows because they cut across the VB olivine, their chemical composition is identical to VB olivine, their orientation corresponds to a common slip system in olivine, and their subgrains are larger than those in VB olivine.

[78] First, the VC olivine appears to postdate formation of the VB olivine. The VC lenses and ribbons are embedded in the VB, which seems inconsistent with the VC forming first. The VC lenses also truncate planar deformation features.

[79] Second, the VC and VB olivine have identical chemical compositions (Figure 4). This implies that they are not related by exsolution or other chemical transformation. The difference in color and BSE brightness (e.g., Figures 2c and 2d) may imply chemical differences (like Fe^{3+} content), but they are too small to register in EMP chemical analyses.

[80] Third, the most common orientation of the VC ribbons is that of an easy deformation system in olivine. The VC ribbons have their long axes near the crystallographic a directions of their host olivine, i.e. in the [100] direction; and the shorter axes of the ribbons are along {021}. This orientation is consistent with slip along {021} planes in the [100] direction, [100]{021}, which is among the easier slip orientations in olivine at high temperatures (~1000°C) and low strain rates [*Cordier*, 2002; *Dunrick et al.*, 2005]. This sort of deformation in olivine has not been reported as a product of shock [*Riemold and Stöffler*, 1978; *Bauer*, 1979; *Stöffler et al.*, 1991].

[81] If the VC ribbons were formed by deformation after the major shock event, how was the original VB olivine transformed to VC? *Reynard et al.* [2006b] suggest that the ribbons might have been melted during deformation. If so, the submicron blebs of iron metal would have a chance to coalesce into larger masses. This would remove the absorption and scattering that produce the brown color, and produce larger grains of iron metal that would be visible in optical micrographs (Figure 2b).

6.6. Later Shock Event

[82] The mosaicism and planar fractures of the VC olivine (Figures 2a and 2d) cannot be explained by this major shock and subsequent deformation, and require a second shock event. The VC olivine is cut by widely spaced planar fractures along {010} and {001} planes, which are a typical product of shock at stage S4 [*Stöffler et al.*, 1991]. These fractures penetrate only slightly into the VB olivine surrounding the VC. So, it seems reasonable to infer that these fractures postdate formation of the VC olivine, and so cannot have been made in the earlier S5 shock event. It is not clear why these fractures do not penetrate far into the VB olivine. Similarly, VC olivine is divided into subgrains, but of much larger grains than in the VB olivine. Such mosaicism is consistent with shock deformation of stage S4 onto undeformed olivine crystals [*Stöffler et al.*, 1991]. If the olivine were already strongly mosaicized, as produced in the earlier S5 shock, it would not be annealed in a later lesser shock. Rather, the presence of the coarser mosaicism of the VC olivine is consistent with annealing during or after the deformation event and a second shock of S4.

[83] It seems unlikely that a Martian sample would record two impact shock events within the last 1.3 Ga: the crystallization age of NWA 2737. However, unlikely it may seem, petrographic relationships clearly suggest two distinct episodes of deformation and shock, and shock at the S4 level does not require a large impactor or resultant crater.

[84] The age of this later S4 shock is not known, as it has not produced a detectable effect in Ar-Ar systematics [*Bogard and Garrison*, 2006]. Lacking real data, one may hypothesize that the S4 shock represents ejection of NWA 2737 from Mars.

6.7. Summary of History

[85] The NWA 2737 meteorite experienced a fairly complex history including at least two shock events. The meteorite was formed, at 1.3 Ga, as an olivine-rich igneous cumulate derived from basaltic magma relatively enriched in incompatible elements [*Beck et al.*, 2006]. This cumulate formed in a fairly large magma body or rapidly emplaced stack of lava flows, so that it cooled slowly enough at its liquidus to allow homogenization of its pyroxenes. Thereafter, cooling was more rapid so as to yield the elongate anorthoclase crystals of the mesostasis. These constraints suggest that the magma body was of moderate size, like a dike or sill, and was not a large pluton. Conditions during this cooling were relatively oxidizing, at ~QFM – 1, which is comparable to oxidation states of the Chassigny and the nakhlites.

[86] Long afterward, at 170 Ma, the rock was involved in a major impact shock event, to stage S5–S6, affected all of the minerals and produced the dark color of the olivine. Deformation followed, possibly in recovery after the major shock event, and brown olivine was deformed along ribbon-shaped zones, possibly to melting, to produce the visually clear areas. Later, the rock was shocked again less severely, to stage S4. The latter shock could have been the ejection of NWA 2737 from Mars, which might be at the common ejection age for nakhlites and Chassigny, ~11 Ma [*Nyquist et al.*, 2001].

[87] NWA 2737 was affected slightly by its residence on Earth. Chemical alteration is limited to slight staining by ferric iron, deposition of calcite along cracks, and slight dissolution of feldspathic glass in the mesostasis and in inclusions. This alteration, although limited in appearance,

profoundly disturbed the Rb-Sr isotopic systematics of the rock [*Misawa et al.*, 2005a] by addition of terrestrial radiogenic Sr. The Sm-Nd system was not affected, and it yields a concordant mineral isochron with a reasonable age [*Misawa et al.*, 2005a].

7. Comparison With Chassigny

[88] There is no question that NWA 2737 is closely related to the Chassigny meteorite [*Beck et al.*, 2006]. Yet, a comparison may be revealing for the geologic histories of both meteorites. As noted here and by *Beck et al.* [2006], NWA 2737 and Chassigny have similar textures (including magmatic inclusions), minerals (including kaersutite amphibole), mineral abundances, element abundance ratios suggesting an origin on Mars, oxygen isotope compositions, crystallization ages, initial Nd isotopic ratios [*Misawa et al.*, 2005a, 2005b], oxygen fugacities during crystallization, trace element abundances and patterns, and features indicative of shock stage S4 or S5 [*Langenhorst and Greshake*, 1999; *Fritz et al.*, 2005]. There are petrologically significant differences; compared to Chassigny, NWA 2737 has a higher Mg/Fe ratio, no plagioclase, mesostasis with variolitic texture, highly colored olivine cut by deformation bands, iron metal in the olivine, and a young Ar-Ar age [*Bogard and Garrison*, 2006].

7.1. Igneous Precursor

[89] Despite these differences, it remains possible that Chassigny and NWA 2737 formed in the same magma body, as permitted by the Nd isotopic initials. One could hypothesize that Chassigny formed closer to the center of the magma body, and so was more affected by late igneous processes. The differences in Mg/Fe and could arise through ''magma metasomatism,'' equilibration of cumulus minerals with evolved magma that flowed through the cumulus pile [e.g., *Irvine*, 1980]. The difference in feldspar mineralogy and composition could conceivably arise in the same process. The differences in feldspar texture, variolitic in NWA 2737 and coarse in Chassigny, could represent different cooling rates within a single body. Formation in a single body would be disproved if one were to uncover significant differences in radioisotope initials or trace element ratios. Proof that the meteorites formed in a single body would be difficult, as many of the crucial clues (like mineral zoning patterns) have been erased.

7.2. Shock History

[90] The greatest differences between NWA 2737 and Chassigny are in their shock features. Both meteorites experienced a major shock event, but to different degrees, and show evidence for a second event.

[91] NWA 2737 and Chassigny experienced major shock events of stage S4–S5 [*Langenhorst and Greshake*, 1999; *Fritz et al.*, 2005], but the effects in the former are more severe. The olivine in Chassigny shows abundant dislocations and subgrain boundaries [*Langenhorst and Greshake*, 1999, Figure 4], and the ''planar fractures'' described by *Langenhorst and Greshake* [1999] may be identical to the planar deformation features reported here. However, the Chassigny olivine shows neither the intense mosaicism of NWA 2737 (Figure 3a) nor any indication of a transformation to a denser polymorph. NWA 2737 is remarkable for its highly colored olivine, which may be caused by the nanophase iron globules in its olivine. Chassigny has neither: Its olivine is green to the human eye [*Floran et al.*, 1978] and contains no nanophase inclusions [*Langenhorst and Greshake*, 1999].

[92] In NWA 2737, these shock effects are ascribed to the event at 0.17 Ga that caused near-total loss of Ar [*Bogard and Garrison*, 2006] and deformation (perhaps to melting) that produced the VC ribbons in olivine. Chassigny preserves no evidence for such a thermal event, and its K-Ar chronometer is concordant with Sm-Nd and Rb-Sr at 1.35 Ga [*Bogard and Garrison*, 1999; *Nyquist et al.*, 2001].

[93] In NWA 2737, fractures that cut only the VC olivine ribbons bespeak a second shock event, of stage S4, after the first shock and formation of the VC ribbons. *Langenhorst and Greshake* [1999] suggest that Chassigny may have experienced a similar second shock, but the evidence is indirect and possibly consistent with a single shock. If real, the second shock is correlated with Chassigny's launch from Mars, as we have done with the second shock in NWA 2737.

8. Olivine Color

[94] NWA 2737 is very similar to Chassigny in mineralogy and composition, yet it appears totally different to the naked eye. In hand sample, Chassigny is light olive green while NWA 2737 is black. In standard thin section Chassigny's olivine is colorless, while that of NWA 2737 is deep brown. The color (i.e., reflectance) of NWA 2737 is explored in a companion paper (Pieters et al., submitted manuscript). Here, we present petrological and mineral-chemical background to help constrain subsequent discussion of the coloration of the olivine in NWA 2737.

[95] Brown olivine is common in Martian meteorites, so our results for NWA 2737 may have broad implications for remote sensing of Mars (Pieters et al., submitted manuscript). Martian meteorites in which brown olivine has been reported include ALHA 77005, LEW 88516, Y-793605, DaG476 and its pairs, NWA 1068, NWA 2046, and SaU 005 and its pairs [*McSween et al.*, 1979; *Ostertag et al.*, 1984; *Steele and Smith*, 1984; *Treiman et al.*, 1994; *Ikeda*, 1994; *Mikouchi and Miyamoto*, 1997; *Taylor et al.*, 2002; *Goodrich*, 2003; *Meyer*, 2003; *Walton et al.*, 2005].

[96] Reports of brown olivine have centered on the lherzolites ALHA 77005 and LEW 88516, though the cause(s) of their color remains unclear. Originally, *Ostertag et al.* [1984] suggested that shock-induced oxidation produced significant levels of Fe^{3+} in the crystal lattice, causing the olivine of ALHA77005 to be brown. Pure Fe^{3+}-Fe^{2+} olivine laihunite [$Fe^{2+}Fe^{3+}{}_2 \bullet (SiO_2)_2$] is itself black. However, *Burns* [1989] later found that those meteorite olivines contain <1% of their iron as Fe^{3+}. *Burns* [1989] and other workers [*Puga et al.*, 1998, 2000; *Ruiz-Cruz et al.*, 1999] suggested that nanophase inclusions of magnetite might be responsible for the brown color. Another possible source of the brown color, by analogy with lunar soils and space weathering [*Noble et al.*, 2001], is nanophase inclusions of iron metal. These papers made the connection between the phenomenon of shock and the occurrence of the brown color, but they could not draw conclusions about

the origin and physical basis for the color (see Pieters et al., submitted manuscript).

[97] On the basis of petrography, two of these mechanisms seem plausible for NWA 2737: Its olivine contains both ferric iron and nanophase inclusions of iron metal. No inclusions of nanophase magnetite have been found. The visually brown olivine and visually colorless olivine have the same chemical composition and (within broad constraints of EMP and SmX) the same calculated abundances of Fe^{3+}. The only differences we observe between brown and clear olivine are at the TEM scale: abundant subgrain boundaries and nanophase iron globules in the former. The subgrain boundaries would contain abundant sites suitable for ferric iron (and other incompatible elements: e.g., *Hiraga et al.* [2004]), which could induce the visual color; the nanophase iron globules by themselves can also induce a visual color [*Noble et al.*, 2001]. Petrography and mineral chemistry for this meteorite do not allow us to determine the cause of the color (but see Pieters et al., submitted manuscript). However, the characteristics of NWA 2737 as discussed in this paper place very important constraints on the physical processes involved, as well as the characteristics of the source region from which these meteorites have been derived.

[98] **Acknowledgments.** We are grateful to the ARES division of NASA Johnson Space Center for access to the EMP and TEM instruments used in this work. C. Schwandt and L. Keller assisted our analyses. Synchrotron micro-XANES measurements at NSLS beamline X26A are supported by DOE grant DOEFG0292ER14244 to S. Sutton, M. Rivers, and A. Lanzirotti (CARS/University of Chicago). Research carried out in part at the National Synchrotron Light Source, Brookhaven National Laboratory, which is supported by the U.S. Department of Energy, Division of Materials Sciences and Division of Chemical Sciences, under contract DE-AC02-98CH10886. Intellectual contributions from D. Stöffler, T. Hiroi, M. Lane, J. Bishop, and J. Sunshine were important for this manuscript, and we are grateful to B. Fectay and C. Bidaut for making NWA 2737 available. McCanta's participation is through a Urey postdoctoral fellowship at the Lunar and Planetary Institute. Treiman's participation is funded in part through the NASA Astrobiology Institute node at Ames Research. Support for this work from NASA grants NNG04GB53G, NNG04GG12G, and NAG5-12687, NAG5-12271, and NAG5-13279 is gratefully acknowledged. We thank Jörg Fritz and an anonymous reviewer for their thoughtful and detailed comments. Lunar and Planetary Institute contribution 1321.

References

Akimoto, S., Y. Matsui, and Y. Sono (1976), High-pressure crystal chemistry of orthosilicates and the formation of the mantle transition zone, in *The Physics and Chemistry of Minerals and Rocks*, edited by R. J. G. Strens, pp. 327–363, John Wiley, Hoboken, N. J.

Andersen, D. J., D. H. Lindsley, and P. M. Davidson (1993), QUILF: A PASCAL program to assess equilibria among Fe-Mg-Mn-Ti oxides, pyroxenes, olivine, and quartz, *Comput. Geosci.*, *19*, 1333–1350.

Ballhaus, C., R. F. Berry, and D. H. Green (1991), High pressure experimental calibration of the olivine-orthopyroxene-spinel oxygen barometer: Implications for the oxidation state of the upper mantle, *Contrib. Mineral. Petrol.*, *107*, 27–40.

Banfield, J. F., D. R. Veblen, and B. F. Jones (1990), Transmission electron microscopy of subsolidus oxidation and weathering of olivine, *Contrib. Mineral. Petrol.*, *106*, 110–123.

Banfield, J. F., M. D. Dyar, and A. V. McGuire (1992), The defect microstructure of oxidized mantle olivine from Dish Hill, California, *Am. Mineral.*, *77*, 977–986.

Bauer, J. F. (1979), Experimental shock metamorphism of mono- and polycrystalline olivine: A comparative study, *Proc. Lunar Planet. Sci. Conf. Xth.*, 2573–2596.

Beck, P., J.-A. Barrat, P. Gillet, I. A. Franchi, R. C. Greenwood, B. Van de Moortèle, B. Reynard, M. Bohn, and J. Cotten (2005), The Diderot meteorite: The second chassignite (abstract), *Lunar Planet. Sci.* [CD-ROM], *XXXVI*, abstract 1326.

Beck, P., P. Gillet, J.-A. Barrat, M. Wadhwa, R. C. Greenwood, I. A. Franchi, M. Bohn, J. Cotten, B. van de Moortèle, and B. Reynard (2006), Petrography and geochemistry of the chassignite Northwest Africa 2737 (NWA 2737), *Geochim. Cosmochim. Acta*, *70*, 2127–2139.

Becker, R. H., and R. O. Pepin (1984), The case for a Martian origin of the shergottites: Nitrogen and noble gases in EETA 79001, *Earth Planet. Sci. Lett.*, *69*, 225–242.

Bogard, D. D., and D. H. Garrison (1999), Argon-39–Argon-40 "ages" and trapped Argon in Martian shergottites, Chassigny, and Allan Hills 84001, *Meteorit. Planet. Sci.*, *34*, 451–573.

Bogard, D. D., and D. H. Garrison (2006), Ar-Ar dating of Martian chassignites, NWA2737 and Chassigny, and nakhlite MIL03346 (abstract), *Lunar Planet. Sci.* [CD-ROM], *XXXVII*, abstract 1108.

Bogard, D. D., and P. Johnson (1983), Martian gases in an Antarctic meteorite?, *Science*, *221*, 651–654.

Burns, R. G. (1989), Olivine alteration phases in shergottite ALHA 77005: Information from 4.2 degrees K Mössbauer spectra (abstract), *Reports of Planetary Geology and Geophysics Program: 1988*, *NASA Tech. Memo. 4130*, 211–212.

Carslaw, H. S., and J. C. Jaeger (1959), *The Conduction of Heat in Solids*, Clarendon, Oxford, U. K.

Chen, Y. L., B. F. Xu, J. G. Chen, and Y. Y. Ge (1992), Fe^{2+} – Fe^{3+} ordered distribution in chromite spinels, *Phys. Chem. Miner.*, *19*, 255–259.

Cordier, P. (2002), Dislocations and slip systems of mantle minerals, in *Plastic Deformation of Minerals and Rocks*, edited by S.-I. Karato and H.-R. Wenk, *Rev. Mineral. Geochem.*, *51*, Mineral. Soc. Am., 137–179, Washington, D. C.

Cosca, M. A., E. J. Essene, and J. R. Bowman (1991), Complete chemical analyses of metamorphic hornblendes: Implications for normalizations, calculated H_2O activities, and thermobarometry, *Contrib. Mineral. Petrol.*, *108*, 472–484.

Delaney, J. S., and M. D. Dyar (2001), Magmatic magnetite in Martian meteorite melt inclusions from Chassigny (abstract), *Meteorit. Planet. Sci.*, *36*, A48.

Delaney, J. S., S. Bajt, M. D. Dyar, S. J. Sutton, G. McKay, and P. Roeder (1996), Comparison of quantitative synchrotron microXANES (SMX): $Fe^{3+}/(Fe^{3+} + Fe^{2+})$ results for amphibole and silicate glass with independent measurements (abstract), *Lunar Planet. Sci.*, *XXVII*, 299–300.

Dunrick, J., A. Legris, and P. Cordier (2005), Influence of crystal chemistry on ideal plastic shear anisotropy in forsterite: First principles calculations, *Am. Mineral.*, *90*, 1072–1077.

Dyar, M. D., A. V. McGuire, and R. D. Ziegler (1989), Redox equilibria and crystal chemistry of coexisting minerals from spinel lherzolite mantle xenoliths, *Am. Mineral.*, *74*, 969–980.

Dyar, M. D., A. V. McGuire, and M. D. Harrell (1992), Crystal chemistry of iron in contrasting styles of metasomatism in the upper mantle, *Geochim. Cosmochim. Acta*, *56*, 2579–2586.

Dyar, M. D., S. V. Martin, S. J. Mackwell, S. Carpenter, C. A. Grant, and A. V. McGuire (1996), Crystal chemistry of Fe^{3+}, H^+, and D/H in mantle-derived augite from Dish Hill: Implications for alteration during transport, in *Mineral Spectroscopy: A Tribute to Roger G. Burns*, edited by M. D. Dyar, C. A. McCammon, and M. Schaefer, *Spec. Publ. Geochem. Soc.*, *5*, 273–289.

Dyar, M. D., E. W. Lowe, C. V. Guidotti, and J. S. Delaney (2002), Fe^{3+} and Fe^{2+} partitioning among silicates in metapelites: A synchrotron micro-XANES study, *Am. Mineral.*, *87*, 514–522.

Dyar, M. D., A. H. Treiman, C. M. Pieters, T. Hiroi, M. D. Lane, and V. O'Connor (2005), MIL03346, the most oxidized Martian meteorite: A first look at petrography, mineral chemistry, and spectroscopy, *J. Geophys. Res.*, *110*, E09005, doi:10.1029/2005JE002426.

Filiberto, J., and H. Nekvasil (2006), Is high-Fe, low-Al Martian parental magma required for the chassignites? An experimental inquiry, *Meteorit. Planet.*, *41*, in press.

Floran, R. J., M. Prinz, P. F. Hlava, K. Keil, C. E. Nehru, and J. R. Hinthorne (1978), The Chassigny meteorite: A cumulate dunite with hydrous amphibole-bearing melt inclusions, *Geochim. Cosmochim. Acta*, *42*, 1213–1229.

Fritz, J., N. Artemieva, and A. Greshake (2005), Ejection of Martian meteorites, *Meteorit. Planet. Sci.*, *40*, 1393–1411.

Goodrich, C. A. (2003), Petrogenesis of olivine-phyric shergottites Sayh al Uhaymir 005 and Elephant Moraine 79001 lithology A, *Geochim. Cosmochim. Acta*, *67*, 373–377.

Goodrich, C. A., C. D. K. Herd, and L. A. Taylor (2003), Spinels and oxygen fugacity in olivine-phyric and lherzolitic shergottites, *Meteorit. Planet. Sci.*, *38*, 1773–1792.

Greshake, A., T. Stephan, and D. Rost (1998), Symplectic exsolution in olivine from the Martian meteorite Chassigny: Evidence for slow cooling under highly oxidizing conditions (abstract), *Lunar Planet. Sci.* [CDROM], *XXIX*, abstract 1069.

Grove, T. L. (1978), Cooling histories of Luna 24 very low Ti (VLT) ferrobasalts: An experimental study, *Proc. Lunar Planet. Sci. Conf. 9th*, 565–684.

Harvey, R. P., and V. E. Hamilton (2005), Syrtis Major as the source of the nakhlite/chassignite Martian meteorites (abstract), *Meteorit. Planet. Sci.*, *40*, suppl. A64, 5165.

Herd, C. D. K. (2003), The oxygen fugacity of olivine-phyric Martian basalts and the components within the mantle and crust of Mars, *Meteorit. Planet. Sci.*, *38*, 1793–1805.

Herd, C. D. K. (2006), Insights into the redox history of the NWA 1068/1110 Martian basalt from mineral equilibria and vanadium oxybarometry, *Am. Mineral.*, *91*, 1616–1627.

Herd, C. D. K., J. J. Papike, and A. J. Brearley (2001), Oxygen fugacity of Martian basalts from electron microprobe oxygen and TEM-EELS analyses of Fe-Ti oxides, *Am. Mineral.*, *86*, 1015–1024.

Herd, C. D. K., L. E. Borg, J. H. Jones, and J. J. Papike (2002a), Oxygen fugacity and geochemical variations in the Martian basalts: Implications for Martian basalt petrogenesis and the oxidation state of the upper mantle, *Geochim. Cosmochim. Acta*, *66*, 2025–2036.

Herd, C. D. K., C. S. Schwandt, J. H. Jones, and J. J. Papike (2002b), An experimental and petrography investigation of Elephant Moraine 79001 lithology A: Implications for its petrogenesis and the partitioning of chromium and vanadium in a Martian basalt, *Meteorit. Planet. Sci.*, *37*, 987–1000.

Hiraga, T., I. M. Anderson, and D. L. Kohlstedt (2004), Grain boundaries as reservoirs of incompatible elements in the Earth's mantle, *Nature*, *427*, 699–703.

Ikeda, Y. (1994), Petrography and petrology of the ALH-77005 shergottite, *Proc. NIPR Symp. Antarct. Meteorit.*, *7*, 9–29.

Irvine, T. N. (1980), Magmatic infiltration metasomatism, double diffusive fractional crystallization and adcumulus growth in the Muskox and other layered intrusions, in *Physics of Magmatic Processes*, edited by R. B. Hargraves, pp. 325–383, Princeton Univ. Press, Princeton, N. J.

Jaeger, J. C. (1968), Cooling and solidification of igneous rocks, in *Basalts*, edited by H. H. Hess and A. Poldervaart, pp. 503–536, Wiley-Intersci., Hoboken, N. J.

Janney, D. E., and J. F. Banfield (1998), Distribution of cations and vacancies and the structure of defects in oxidized intermediate olivine by atomic-resolution TEM and image simulation, *Am. Mineral.*, *83*, 799–810.

Johnson, M. C., M. J. Rutherford, and P. C. Hess (1991), Chassigny petrogenesis: Melt compositions, intensive parameters, and water contents of Martian (?) magmas, *Geochim. Cosmochim. Acta*, *55*, 349–366.

Karner, J., J. J. Papike, and C. K. Shearer (2003), Olivine from planetary basalts: Chemical signatures that indicate planetary parentage and those that record igneous setting and process, *Am. Mineral.*, *88*, 806–816.

Kitamura, M., S. Kondoh, N. Morimoto, G. H. Miller, G. R. Rossman, and A. Putnis (1987), Planar OH-bearing defects in mantle olivine, *Nature*, *328*, 143–145.

Langenhorst, F., and A. Greshake (1999), A transmission electron microscope study of Chassigny: Evidence for strong shock metamorphism, *Meteorit. Planet. Sci.*, *34*, 43–48.

Li, Z., J. Y. Ping, M. Z. Jin, and M. L. Liu (2002), Distribution of Fe^{2+} and Fe^{3+} and next-nearest neighbour effects in natural chromites: Comparison between results of QSD and Lorentzian doublet analysis, *Phys. Chem. Miner.*, *29*, 485–494.

Longhi, J., and V. Pan (1989), The parent magmas of the SNC meteorites, *Proc. Lunar Planet. Sci. Conf. 19th*, 451–464.

McCanta, M. C., M. J. Rutherford, and J. H. Jones (2004a), An experimental study of rare Earth element partitioning between a shergottite melt and pigeonite: Implications for the oxygen fugacity of the Martian interior, *Geochim. Cosmochim. Acta*, *68*, 1943–1952.

McCanta, M. C., M. D. Dyar, M. J. Rutherford, and J. S. Delaney (2004b), Iron partitioning between basalt and clinopyroxene as a function of oxygen fugacity, *Am. Mineral.*, *89*, 1685–1693.

McGuire, A. V., M. D. Dyar, and J. E. Nielson (1991), Metasomatic oxidation of upper mantle peridotite, *Contrib. Mineral. Petrol.*, *109*, 252–264.

McSween, H. Y., Jr., L. A. Taylor, and E. M. Stolper (1979), Allan Hills 77005: A new meteorite type found in Antarctica, *Science*, *204*, 1201–1203.

Melosh, H. J., A. H. Treiman, and R. A. F. Greive (1983), Olivine composition glass in the Chassigny meteorite: Implications for shock history (abstract), *Eos Trans. AGU*, *64*, 254.

Meyer, C. (2003), *Mars Meteorite Compendium*, *Johnson Space Center Rep. JSC27672*, revision B. (Available at http://curator.jsc.nasa.gov/antmet/mmc/mmc.htm)

Mikouchi, T. (2005), Comparative mineralogy of Chassigny and NWA 2737: Implications for the formation of chassignite igneous body (s) (abstract), *Meteorit. Planet. Sci.*, *40*, suppl. A102, 5240.

Mikouchi, T., and M. Miyamoto (1997), Yamato Y-793605: A lherzolite shergottite from Japanese Antarctic meteorite collection, *Antarct. Meteorit. Res.*, *10*, 41–60.

Mikouchi, T., Y. Ikiko, and M. Miyamoto (2000), Symplectic exsolution in olivine from the Nakhla Martian meteorite, *Meteorit. Planet. Sci.*, *35*, 937–942.

Mikouchi, T., A. Monkawa, E. Koizumi, J. Chokai, and M. Miyamoto (2005), MIL03346 nakhlite and NWA 2737 (''Diderot'') chassignite: Two new Martian cumulate rocks from hot and cold deserts, *Lunar. Planet Sci.*, *XXXVI*, abstract 1944.

Misawa, K., C.-Y. Shih, Y. Reese, L. E. Nyquist, and J.-A. Barrat (2005a), Rb-Sr and Sm-Nd isotopic systematics of NWA 2737 chassignite (abstract), *Meteorit. Planet. Sci.*, *40*, suppl. A104, 5200.

Misawa, K., C.-Y. Shih, Y. Reese, and L. E. Nyquist (2005b), Crystallization age and source signature of Chassigny, *Lunar Planet. Sci.* [CD-ROM], *XXXVI*, abstract 1698.

Monkawa, A., T. Mikouchi, E. Koizumi, J. Chokai, and M. Miyamoto (2004), Fast cooling history of the Chassigny Martian meteorite, *Lunar Planet. Sci.* [CD-ROM], *XXXV*, abstract 1535.

Mottana, A., A. Marcelli, G. Cibin, and M. D. Dyar (2002), X-ray absorption spectroscopy of the micas, *Rev. Mineral. Geochem.*, *46*, 371–412.

Noble, S. K., C. M. Pieters, L. A. Taylor, R. V. Morris, C. C. Allen, D. A. McKay, and L. P. Keller (2001), The optical properties of the finest fraction of lunar soil: Implications for space weathering, *Meteorit. Planet. Sci.*, *36*, 31–42.

Nyquist, L. E., D. D. Bogard, C.-Y. Shih, A. Greshake, D. Stöffler, and O. Eugster (2001), Ages and geological histories of Martian meteorites, in *Chronology and Evolution of Mars*, edited by R. Kallenbach, J. Geiss, and W. K. Hartmann, pp. 105–164, Springer, New York.

O'Neill, H. St. C., C. A. McCammon, D. Canil, D. C. Rubie, C. R. Ross II, and F. Seifert (1993), Mössbauer spectroscopy of mantle transition zone phases and determination of minimum Fe^{3+} content, *Am. Mineral.*, *78*, 456–460.

Osborne, M. D., M. E. Fleet, and G. M. Bancroft (1981), Fe^{2+}-Fe^{3+} ordering in chromite and Cr-bearing spinels, *Contrib. Mineral. Petrol.*, *77*, 251–255.

Ostertag, R., G. Amthauer, H. Rager, and H. Y. McSween Jr. (1984), Fe^{3+} in shocked olivine crystals of the ALHA 77005 meteorite, *Earth Planet. Sci. Lett.*, *67*, 162–166.

Papike, J. J., J. M. Karner, and C. K. Shearer (2003), Determination of planetary basalt parentage: A simple technique using the electron microprobe, *Am. Mineral.*, *88*, 469–472.

Puga, E., E. Jagoutz, J. M. Nieto, A. Diaz de Federico, and M. D. Ruiz-Cruz (1998), On the origin of the brown color in ALHA 77005 olivine, *Lunar Planet. Sci.*, *XXIX*, abstract 1375.

Puga, E., J. M. Nieto, and A. Diaz de Federico (2000), Contrasting P–T paths in eclogites of the Betic ophiolitic association, Mulhacén complex, southeastern Spain, *Can. Mineral.*, *38*, 1137–1161.

Reynard, B., B. van Moortèle, P. Beck, and P. Gillet (2006a), Shock-induced transformations in olivine of the chassignite NWA 2737, *Lunar Planet. Sci.* [CD-ROM], *XXXVII*, abstract 1837.

Reynard, B., P. Beck, J.-A. Barrat, and M. Bohn (2006b), Pyroxene crystal chemistry and the late cooling history of NWA 2737, *Lunar Planet. Sci.*, *XXXVII*, abstract 1963.

Riemold, W. U., and D. Stöffler (1978), Experimental shock metamorphism of dunite, *Proc. Lunar Planet. Sci. Conf. 9th*, 2805–2824.

Rubin, A., E. R. D. Scott, and K. Keil (1997), Shock metamorphism of enstatite chondrites, *Geochim. Cosmochim. Acta*, *61*, 847–858.

Ruiz-Cruz, M. D., E. Puga, and J. M. Nieto (1999), Silicate and oxide exsolution in pseudo-spinifex olivine from meta-ultramafic rocks of the Betic Ophiolitic Association: A TEM study, *Am. Mineral.*, *84*, 1915–1924.

Russell, S. S., M. Zolensky, K. Righter, L. Folco, R. Jones, H. C. Connolly Jr., M. M. Grady, and J. N. Grossman (2005), The Meteoritical Bulletin, 89, *Meteorit. Planet. Sci.*, *40*, suppl., A201–A263.

Sack, R. O., and M. S. Ghiorso (1991a), Chromian spinels as petrogenetic indicators: Thermodynamics and petrologic applications, *Am. Mineral.*, *76*, 827–847.

Sack, R. O., and M. S. Ghiorso (1991b), An internally consistent model for the thermodynamic properties of Fe-Mg-titanomagnetite-aluminate spinels, *Contrib. Mineral. Petrol.*, *106*, 474–505.

Schmitt, R. T. (2000), Shock experiments with the H6 chondrite Kernouve: Pressure calibration of microscopic shock effects, *Meteorit. Planet. Sci.*, *35*, 545–560.

Steele, I., and J. V. Smith (1984), Achondrite ALHA77005: Alteration of chromite and olivine, *Meteoritics*, *19*, 121–133.

Stöffler, D., K. Keil, and E. R. D. Scott (1991), Shock metamorphism of ordinary chondrites, *Geochim. Cosmochim. Acta*, *55*, 3845–3867.

Stöffler, D., K. Keil, and E. R. D. Scott (1992), Shock classification of ordinary chondrites: New data and interpretations (abstract), *Meteoritics*, *27*, 292–293.

Szymanski, A., A. El Goresy, F. E. Brenker, and H. Palme (2003), Application of the Fe-Ti thermobarometer/oxybarometer to Nakhla and Y000593, paper presented at the NIPR Symposium, 2003, Nat. Inst. of Polar Res., Tokyo, 3–5 Sept.

Taylor, L. A., et al. (2002), Martian meteorite Dhofar 019: A new shergottite, *Meteorit. Planet. Sci.*, *37*, 1107–1128.

Treiman, A. H. (1993), The parental magma of the Nakhla (SNC) achondrite, inferred from magmatic inclusions, *Geochim. Cosmochim. Acta*, *57*, 4753–4767.

Treiman, A. H. (1995), A petrographic history of Martian meteorite ALH84001: Two shocks and an ancient age, *Meteoritics*, *30*, 294–302.

Treiman, A. H. (2005), The nakhlite Martian meteorites: Augite-rich igneous rock from Mars, *Chemie der Erde*, *65*, 203–270.

Treiman, A. H., G. A. McKay, D. D. Bogard, D. W. Mittlefehldt, M.-S. Wang, L. Keller, M. E. Lipschutz, M. M. Lindstrom, and D. Garrison (1994), Comparison of the LEW88516 and ALHA77005 Martian meteorites: Similar but distinct, *Meteoritics*, *29*, 581–592.

Treiman, A. H., J. D. Gleason, and D. D. Bogard (2000), The SNC meteorites are from Mars, *Planet. Space Sci.*, *48*, 1213–1230.

von Seckendorf, V., and H. St. C. O'Neill (1993), An experimental study of Fe-Mg partitioning between olivine and orthopyroxene at 1173, 1273 and 1423 K and 1.6 GPa, *Contrib. Mineral. Petrol.*, *113*, 197–207.

Wadhwa, M., and G. Crozaz (1995), Trace and minor elements in minerals of nakhlites and Chassigny: Clues to their petrogenesis, *Geochim. Cosmochim. Acta*, *59*, 3629–3645.

Walton, E. L., J. G. Spray, and R. Bartoschewitz (2005), A new Martian meteorite from Oman: Mineralogy, petrology, and shock metamorphism of olivine-phyric basaltic shergottite Sayh al Uhaymir 150, *Meteorit. Planet. Sci.*, *40*, 1195–1214.

Wen, S., and H. Nekvasil (1994), SOLVCALC: An interactive graphics program package for calculating the ternary feldspar solvus and for two-feldspar geothermometry, *Comput. Geosci.*, *20*, 1025–1040.

Wilke, M., F. Farges, P.-E. Petit, G. E. Brown Jr., and F. Martin (2001), Oxidation state and coordination of Fe in minerals: An Fe *K*-XANES spectroscopic study, *Am. Mineral.*, *86*, 714–730.

Wivel, C., and S. Mørup (1981), Improved computational procedure for evaluation of overlapping hyperfine parameter distributions in Mössbauer spectra, *J. Phys. E Sci. Instrum.*, *14*, 605–610.

Wood, B. J. (1991), Oxygen barometry of spinel peridotites, in *Oxide minerals: Petrologic and Magnetic Significance*, edited by D. H. Lindsley, *Rev. Mineral.*, *14*, 417–431.

M. D. Dyar, Department of Astronomy, Mount Holyoke College, South Hadley, MA 01075, USA.

M. McCanta and A. H. Treiman, Lunar and Planetary Institute, 3600 Bay Area Blvd., Houston, TX 77058, USA. (treiman@lpi.usra.edu)

S. K. Noble, ARES Division, Johnson Space Center, Houston, TX 77058, USA.

C. M. Pieters, Department of Geological Sciences, Brown University, 324 Brook Street, Providence, RI 02912, USA.